MONTE CARLO SIMULATIONS OF GLOBULAR CLUSTER EVOLUTION. V. BINARY STELLAR EVOLUTION

SOURAV CHATTERJEE[1], JOHN M. FREGEAU[2,3], STEFAN UMBREIT[1], AND FREDERIC A. RASIO[1]
[1] Department of Physics and Astronomy, Northwestern University, Evanston, IL 60208, USA
[2] Kavli Institute for Theoretical Physics, UCSB, Santa Barbara, CA 93106, USA

ABSTRACT

We study the dynamical evolution of globular clusters containing primordial binaries, including full single and binary stellar evolution using our Monte Carlo cluster evolution code updated with an adaptation of the single and binary stellar evolution codes SSE and BSE from Hurley et al. We describe the modifications that we have made to the code. We present several test calculations and comparisons with existing studies to illustrate the validity of the code. We show that our code finds very good agreement with direct *N*-body simulations including primordial binaries and stellar evolution. We find significant differences in the evolution of the global properties of the simulated clusters using stellar evolution compared with simulations without any stellar evolution. In particular, we find that the mass loss from the stellar evolution acts as a significant energy production channel simply by reducing the total gravitational binding energy and can significantly prolong the initial core contraction phase before reaching the binary-burning quasi-steady state of the cluster evolution. We simulate a large grid of models varying the initial cluster mass, binary fraction, and concentration parameter, and we compare properties of the simulated clusters with those of the observed Galactic globular clusters (GGCs). We find that simply including stellar evolution in our simulations and assuming the typical initial cluster half-mass radius is approximately a few pc independent of mass, our simulated cluster properties agree well with the observed GGC properties such as the core radius and the ratio of the core radius to the half-mass radius. We explore in some detail qualitatively different clusters in different phases of their evolution and construct synthetic Hertzsprung–Russell diagrams for these clusters.

Key words: binaries: general – blue stragglers – Galaxy: kinematics and dynamics – globular clusters: general – methods: numerical

Online-only material: color figures

1. INTRODUCTION

Star clusters in general, and the Galactic globular clusters (GGCs) in particular, have been studied extensively for many years. As tracers of the galactic potential, their dynamical history tells us something about the formation and evolution of our Galaxy. As dense stellar environments, their interesting constituent populations (including, e.g., blue straggler stars, cataclysmic variables, and low-mass X-ray binaries) inform our understanding of binary stellar evolution through its interaction with dynamics. The study of the evolution of globular and other dense star clusters has had a somewhat long and varied history (e.g., Heggie & Hut 2003). Before observations showed that globular clusters contained dynamically significant number of binaries, theoretical efforts focused on understanding the process of core collapse and the ensuing post-collapse evolution driven by three-body binary formation. Once it became clear in the early 1990s from observations that clusters contained a sufficient number of binaries such that they must have been born with substantial "primordial" populations, theory emphasized properties of clusters in the "binary burning" phase, in which the cluster core is supported against collapse by super-elastic dynamical scattering interactions of binary stars. More recently it has been realized that pure point-mass interactions of binaries result in equilibrium cluster core radii in the binary burning phase that are a factor of ~10 smaller than what is observed, and therefore many efforts have focused on alternative cluster energy sources such as central intermediate-mass black holes, expedited stellar mass loss from compact object formation via collisions,

or prolonged mass segregation of compact objects (Heggie et al. 2006; Fregeau & Rasio 2007; Trenti 2006; Chatterjee et al. 2008; Merritt et al. 2004). In a similar vein, recent theoretical work, combined with observations showing that the core binary fraction in many clusters is fairly low ($\lesssim$10%), suggests that clusters may be born with remarkably low binary fractions of just a few percent (Fregeau et al. 2009). Such a small primordial binary fraction would be surprising since observations of young stars suggest that star formation yields binary fractions on the order of ~50% (Duquennoy & Mayor 1991; Fischer & Marcy 1992). Clearly, our understanding of globular cluster evolution has changed considerably over the past few decades, much of which has been driven by numerical simulations.

Among computational tools for studying the dynamical evolution of star clusters, the Hénon Monte Carlo (MC) technique (Hénon 1971a, 1971b) represents a balanced compromise between precision and speed. The MC method allows for a star-by-star realization of the cluster, with its *N* mass shells representing the *N* stellar objects in the cluster (either single or binary stars). It assumes, most importantly, spherical symmetry and diffusive two-body relaxation, allowing time integration on a relaxation timescale, and a computational cost that scales as *N* log *N*. We have developed our Hénon MC cluster evolution code (which we call CMC, for "Cluster Monte Carlo") over the past decade (Joshi et al. 2000, 2001; Fregeau et al. 2003; Fregeau & Rasio 2007; henceforth Papers I, II, III, and IV, respectively). Since it allows for a star-by-star description of the cluster at each timestep, it is relatively easy to add physical processes beyond two-body relaxation to the code. We have previously added the effects of a Galactic tidal field, dynamical scattering interactions of binary star systems, and physical collisions between

---
[3] Chandra/Einstein Fellow.

stars. In this paper, we describe the addition of stellar evolution of single and binary star systems. Many stars in a cluster evolve internally on a timescale shorter than the age of the cluster. At early times, they may lose a substantial fraction of their mass via stellar winds. At later times, they may evolve off the main sequence, changing their masses and radii (and hence collision cross section), and possibly receiving systemic velocity kicks when they become compact objects. Since the binding energy of binary stars is an important fuel source that can postpone the deep core collapse of star clusters, stellar evolution of binary systems directly affects their global evolution. Conversely, the properties of the cluster environment feed back on stellar evolution, modifying the evolutionary pathways of binary systems and the properties and number of interesting binary systems relative to the low-density Galactic field (e.g., X-ray binaries; Ivanova et al. 2006, 2008).

Previous cluster evolution studies that include stellar evolution have improved our understanding of the global evolution of clusters greatly, identifying several distinct stages of evolution. At early times, as the stars are forming and the most massive stars have already begun nuclear burning, the cluster loses mass through residual gas expulsion and stellar winds, resulting in cluster expansion during the first few Myr of evolution (Hurley et al. 2001, 2002). Shortly thereafter, if a runaway collision scenario is avoided (e.g., Freitag et al. 2006a), two-body relaxation dominates, resulting in a fairly long-lived (from a few to tens of Gyr) phase of core contraction. Once the core density becomes high enough for the energy generated in binary scattering interactions to balance the energy carried out of the core by two-body relaxation, a potentially *very* long-lived (up to tens of Hubble times or more) phase of "binary burning" ensues (e.g., Hurley 2007; Fregeau & Rasio 2007). Once the population of binaries is exhausted in the core, the cluster goes into deep core collapse. In the classical, point-mass limit, deep core collapse is arrested by the formation of a "three-body binary" and followed by a phase of gravothermal oscillations (Heggie & Hut 2003). However, three-body binary formation may be inhibited by stellar collisions in sufficiently young and massive clusters (Freitag et al. 2006b).

With the exception of a few recent simulations, most numerical studies that include stellar evolution have either been limited in the number of stars they can treat or have adopted a narrow initial mass function (IMF) with very simplified stellar evolution recipes (e.g., Giersz 1998; Giersz & Spurzem 2000; Joshi et al. 2000, 2001; Fregeau et al. 2003; Fregeau & Rasio 2007). Stars in star clusters are born with a range of masses up to $\sim 100\,M_\odot$, and down to at least the hydrogen-burning limit (e.g., Salpeter 1955; Miller & Scalo 1979; Kroupa 2001), so one should evolve the full spectrum of stellar masses as realistically as possible to properly treat the influence of stellar evolution on global cluster evolution. Emphasis has recently been placed on comparing observed properties of GGCs with theoretical predictions. Comparison of observed cluster structural properties with theory (e.g., Hurley 2007; Fregeau & Rasio 2007) suggests that either an additional energy source is "puffing" up cluster cores (Mackey et al. 2008; Trenti et al. 2007a; Chatterjee et al. 2008), or perhaps the clusters are not in the expected evolutionary states, namely binary burning (Fregeau 2008). For example, recent *N*-body simulations by Hurley (2007) show that the core contraction phase can last a Hubble time, resulting in a cluster core radius that is larger than one would expect were the cluster in the binary burning phase. In these simulations, the core contraction phase is prolonged by mass loss from stellar evolution.

Clearly, stellar evolution may be an important component in globular cluster evolution.

To more properly treat stellar evolution, we have recently coupled to CMC the stellar evolution recipes of Hurley et al. (2000, 2002, hereafter referred to as SSE and BSE, respectively). We choose SSE and BSE for ease of implementation, and for more direct comparisons with *N*-body calculations, which commonly use the same software packages to treat stellar evolution. In Section 2, we describe the implementation of stellar evolution in our code. In Section 3, we validate it by comparing with existing cluster evolution calculations in the literature. In Section 4, we demonstrate the importance of stellar evolution by comparing simulations that do not include it. In Section 5, we apply our newly updated code to the evolution of a large grid of cluster models, highlighting typical behavior and comparing with observations. Finally, in Section 6, we summarize and conclude.

2. METHOD

CMC treats a number of important physical processes, including two-body relaxation, the tidal effects of a host galaxy, strong binary–binary (BB) and binary–single (BS) scattering interactions, and direct physical collisions between stars (Paper IV). Here, we describe the recent addition of SSE and BSE (Hurley et al. 2000, 2002) to treat stellar evolution of single and binary stars.

2.1. Stellar Evolution

For ease of implementation and for more direct comparisons with direct *N*-body, we use the SSE and BSE stellar evolution routines, as described in detail in Hurley et al. (2000, 2002). For single stars, SSE comprises analytic functional fits to theoretically calculated stellar evolution tracks as a function of metallicity and mass. Binary star systems are treated using BSE, which uses the same fitting formulae for each star, but with treatments of physics relevant to binaries, including stable and unstable mass transfer, common envelope evolution, magnetic braking, tidal coupling, and the effects of neutron star and black hole birth kicks. Thus, BSE is in effect a superset of routines which can treat binary stellar evolution and calls the SSE routines to evolve the individual binary components. To simplify our discussion we refer to SSE and BSE collectively as BSE with the understanding that single stars are evolved using SSE and binary stellar evolution is treated using BSE.

As described above, CMC allows for a star-by-star description of the cluster at every timestep, allowing for the inclusion of additional physics. The stellar properties of binary and single stars are updated in step with dynamics via function calls to the BSE library. As described in detail in Papers I–IV, CMC uses a shared timestep which must be set as small as the smallest characteristic timescale for each physical process. We set the characteristic timescale for stellar evolution to the timescale for the cluster to lose a fraction of 0.001 of its current total mass. In this way, any cluster expansion from stellar evolutionary mass loss is properly resolved.

One aspect of our BSE implementation requires special mention, however. The evolution of high-mass stars ($\gtrsim 100\,M_\odot$) is rather uncertain and can vary greatly depending on the wind mass-loss prescription. These high-mass stars are also quite rare and short-lived, so observational constraints are limited. In BSE, stars with mass $>100\,M_\odot$ are evolved as if they were $100\,M_\odot$

stars. When their dynamical properties are returned from BSE, their original ($>100\,M_\odot$) masses are returned.

2.2. Collisions

As described in Paper IV, collisions are treated in the sticky-sphere approximation, which was shown to be remarkably accurate for the velocity dispersions found in globular clusters (Freitag et al. 2006a, 2006b). When two stars collide, their properties (e.g., stellar type and effective age) are set according to the BSE merger matrix and prescriptions as described in Hurley et al. (2002). In CMC, this is implemented in the following simple way. The two stars are passed to BSE as a very tight, eccentric binary with nearly zero pericenter distance and evolved for a very short time until they merge. The properties of the merger product are then naturally set within BSE and returned to CMC as a single star. BSE by default assumes full mixing of nuclear fuel during a collision involving main-sequence stars (MSSs). We adopt this same rejuvenation prescription for the simulations presented in this paper, but note that the amount of mixing in the collision product should depend on the details of the interaction parameters leading to the collision, as well as the evolutionary stages of the collision progenitors (e.g., Lombardi et al. 1995, 1996, 2002; Sills et al. 1997, 2001). In fact, using detailed smoothed particle hydrodynamics (SPH) calculations, it is found that the amount of mixing as a result of a collision may be minimal, especially for collisions involving evolved stars (Lombardi et al. 1995, 1996).

2.3. Tidal Truncation Treatment

Globular clusters are not isolated systems, but are in fact subject to the tidal field of their host galaxy. The assumption of spherical symmetry inherent in MC codes like CMC does not allow for a direct calculation of stellar loss at the tear-drop-shaped tidal boundary. Instead, MC codes employ an effective tidal mass-loss criterion that attempts to match the tidal mass loss found in direct N-body simulations. Since stars are lost from the tidal boundary on a dynamical timescale and MC codes operate on the (much longer) relaxation timescale, the appropriate effective criterion is not obvious. There have been two main suggestions in the literature for the appropriate tidal truncation criterion. Perhaps the most natural one is to immediately strip any star whose apocenter (r_a) lies outside the Roche lobe radius of the cluster (which we call the tidal radius, r_t):

$$r_a > r_t . \qquad (1)$$

This "apocenter criterion" has been used exclusively in CMC previously (Papers I–IV). Earlier, in the absence of large-N direct N-body simulations, comparisons were made with two-dimensional (2D) Fokker–Plank models and the apocenter criterion showed excellent agreement (for details see Papers I and II).

Another simple criterion is the "energy criterion," in which any star with a specific orbital energy above some critical energy is immediately stripped:

$$E_{\rm orb} > \phi_t , \qquad (2)$$

where ϕ_t is the cluster potential at the tidal radius (Spitzer 1987). However, a stellar orbit that instantaneously satisfies the above criterion may still remain bound if it is scattered back to a lower energy orbit before it can escape. To account for this effect, a less obvious but empirically validated correction factor to the energy criterion above is suggested by Giersz et al. (2008):

$$E_{\rm orb} > \alpha \phi_t , \qquad (3)$$

where α is an N-dependent parameter given by

$$\alpha = 1.5 - 3 \left[\frac{\ln(\gamma N)}{N} \right]^{1/4} . \qquad (4)$$

We have re-examined and tested these two criteria (Equations (1) and (3)) for tidal stellar loss to determine which one agrees better with the latest results from direct N-body simulations. Baumgardt & Makino (2003) study in detail the tidal dissolution timescales of a cluster in a tidal field varying the initial number of stars and the initial mass of the cluster. We have repeated a large subset of this extensive study of tidal disruption using CMC with both tidal truncation criteria and compared the results.

We followed the exact same prescription for setting up the initial conditions of the clusters as described in Baumgardt & Makino (2003). Each cluster in this set of runs is assumed to have a circular orbit around the Galactic center with radius $R_G = 8.5$ kpc. A logarithmic potential ($\phi(R_G) = V_G^2 \ln R_G$) for the galaxy is assumed with circular velocity $V_G = 220\,{\rm km\,s^{-1}}$ to calculate the tidal radius. The initial position and velocity of each star of the cluster are chosen from a King model distribution function with central concentration parameter $W_0 = 7$. The initial virial radius (r_v) is adjusted in such a way that the King tidal radius is equal to the tidal radius of the galactic field calculated according to

$$r_t = \left(\frac{Gm_c}{2V_G^2} \right)^{1/3} R_G^{2/3} , \qquad (5)$$

where m_c is the cluster mass (Baumgardt & Makino 2003). The initial masses of the stars are chosen according to Kroupa (2001, their Equations (1) and (2); henceforth, simply referred to as K01 without the equation numbers) mass function in the range 0.1–$15\,M_\odot$. We vary the initial number of stars in the clusters between 16×10^3 and 10^6. There are no primordial binaries in these simulations. We use $\gamma = 0.02$ (see Paper IV, Equations (4) and (5)) in the Coulomb logarithm for these simulations.

Figure 1 shows the evolution of the bound mass in a cluster in the standard Galactic tidal field as described above. We find that the energy criterion results agree better with the direct N-body results, when available from Baumgardt & Makino (2003). The agreement is much poorer when using the apocenter criterion. For example, for the direct N-body run with initial $N = 64 \times 10^3$, the time when the cluster loses 80% of its initial mass is ≈ 11 Gyr. Using CMC with the energy criterion this value is ≈ 10 Gyr, whereas with the apocenter criterion the same cluster does not lose 80% of its initial mass within 20 Gyr, the integration stopping time.

Since the energy criterion originally suggested by Giersz et al. (2008) gives significantly better agreement with existing direct N-body results (Figure 1; see also more detailed comparisons in Section 3), we adopt the energy criterion here, in contrast to what was used in our earlier works (Papers II – IV), unless otherwise mentioned.

One should note, however, that the cluster mass range where direct N-body results are available is not representative of the actual GGC population. Since no direct N-body results exist
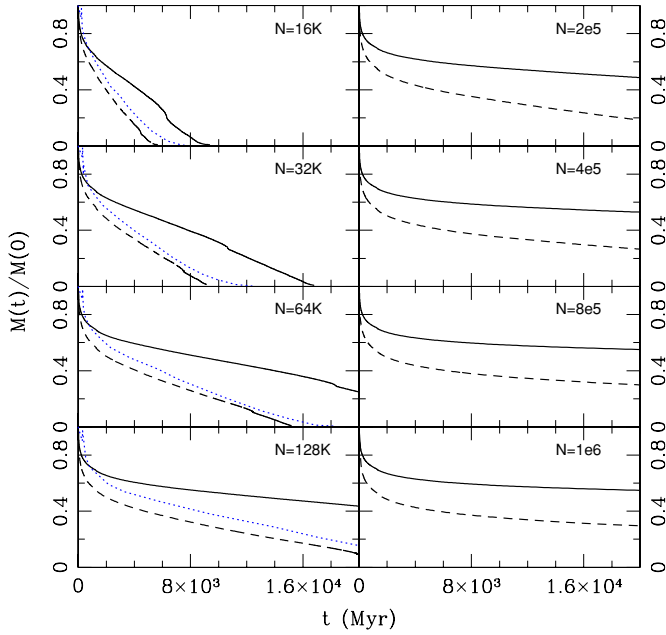
Figure 1. Evolution of the total cluster mass for clusters with various initial number of stars and masses. In each case, a Galactocentric distance $r_G = 8.5$ kpc and a standard Galactic tidal field are assumed. The initial number of stars (N) is noted in each panel. The solid black line and the dashed black line in each panel show CMC results with the apocenter criterion and energy criterion, respectively. The dotted blue lines in the first four panels show the NBODY4 results for the same initial clusters for comparison. The NBODY4 data are taken from the simulations described in Baumgardt & Makino (2003). Similar simulations using NBODY4 do not exist for a higher N. In each case, the energy criterion leads to a higher mass-loss rate than the apocenter criterion. When available, the results using the energy criterion agree better with the direct N-body results.

(A color version of this figure is available in the online journal.)

for more massive clusters, it is not possible at present to determine which approximation is more accurate for larger N. Nevertheless, Heggie & Giersz (2009) have confirmed that the present-day mass-loss rate from NGC6397 ($N \sim 10^5$) using an MC model with the energy criterion agrees well with their direct N-body model for the same cluster during its last ~ 1 Gyr evolution.

The two criteria above are treated as initial options in CMC and either one can be selected at the beginning of a simulation. At each timestep, the amount of mass lost is calculated using the chosen criterion in an iterative way to obtain the bound mass (see Paper II for details).

3. COMPARISON WITH DIRECT N-BODY RESULTS

In this section, we validate our treatment of stellar evolution by comparing with results from previously published studies using the popular direct N-body code NBODY4 (Aarseth 2003). Since the direct N-body simulations make few approximating assumptions, we treat them as a standard for validation.

One of the largest simulations treating all relevant physical effects including primordial binaries and stellar evolution was performed by Hurley et al. (2007) and Hurley (2007). In particular, they studied the evolution of the core properties, binary number fraction in the core as well as in the full cluster, and the evolution of the bound number of stars. Since both these works present data from a common set of simulations we henceforth collectively call them Hurley07.

3.1. Initial Conditions

We choose from Hurley07 the simulations with a number $N_i = 10^5$ initial objects (the largest initial N_i in their set of simulations), with primordial binary fractions $f_b = 5\%$ and $f_b = 10\%$ (their K100-5 and K100-10 models, respectively). Throughout this work we count each binary as one object. Thus a cluster with $N_i = 10^5$ and $f_{b,i} = 5\%$ initially has 95,000 single stars and 5000 binaries. We simulate clusters using CMC with initial conditions as close as possible to the Hurley07 simulations mentioned above. The initial stellar positions and velocities are chosen from a virialized Plummer sphere. The stellar masses for the single stars are chosen from the IMF presented in Kroupa et al. (1993, Equation (14)) in the range 0.1–$50\,M_\odot$. The binary masses and their orbital properties, such as the semimajor axes and eccentricities are directly obtained from Hurley07 (private communication). Although the binary masses and their orbital properties are directly imported, their initial positions are not. These binaries are randomly inserted in the cluster. For each set of simulations we use two different initial seed values to create the velocities, positions, and single star masses, and obtain two realizations of the same initial cluster.

Metallicity is fixed at $z = 0.001$. Each cluster has an initial virial radius $r_v = 8.5$ pc which corresponds to a Roche-filling cluster with tidal radius $r_t \sim 50$ pc, consistent with a Galactic tidal field with a Galactic rotation speed 220 km s^{-1} at a Galactocentric distance 8.5 kpc (for a detailed description see Hurley 2007, and references therein). We call these simulations `hcn1e5b5` and `hcn1e5b10`, respectively (Table 1).

Throughout this section for comparison with direct N-body results we use $\gamma = 0.02$ in the Coulomb logarithm. Following the default setup for BSE used in NBODY4 black hole birth kicks are not considered. Neutron star birth kicks are drawn from a Maxwellian distribution with velocity dispersion $\sigma = 190$ km s^{-1} (Hansen & Phinney 1997).

3.2. Comparison of Results

For the global evolution of a dense cluster, the evolution of the core is extremely important since throughout the evolution the global properties of the cluster are determined by the balance of energy in and out of the core. In addition, the core radius (r_c) is an observable structural property of a cluster. The evolution of r_c is one of the most convenient theoretical ways to characterize the distinct phases of a cluster's evolution. Thus, a basic test for the validity of a cluster simulation is to compare the evolution of the core radius (r_c) and the ratio of the core to half-mass radius (r_c/r_h).

Note that for all our simulated clusters in this work, r_c is the density-weighted core radius (Casertano & Hut 1985) commonly used in N-body simulations, unless otherwise specified. This is not a directly observable quantity and can differ from the observed r_c by a factor of a few (Hurley 2007; Trenti et al. 2010). To be consistent in our comparisons with direct N-body results, in this section we use the definition of r_c as used in NBODY4 (Trenti et al. 2007b, Equation (6)) which is a variant of the density-weighted core radius in Casertano & Hut (1985).

Figure 2 shows the evolution of r_c for run `hcn1e5b5` (Table 1) and K100-5 in Hurley07. The scale-free quantity r_c/r_h is also plotted for each run. The core radius expands due to stellar evolution mass loss during the first ~ 200 Myr. The core then contracts at a steady rate until a short time after $\sim 1.5 \times 10^4$ Myr. The core radius then attains a relatively steadier value as

Table 1
Initial Conditions for Comparison Runs with Hurley07

Name	N	$M\,(10^4\,M_\odot)$	Profile	IMF	r_t (pc)	r_v (pc)	f_b
hcn1e5b5	10^5	5	Plummer	K93[a] [0.1, 50] $M_\odot$	51	8.5	0.05
hcn1e5b10	10^5	5	Plummer	K93 [0.1, 50] $M_\odot$	51	8.5	0.1

**Note.** [a] Kroupa mass function as described in Kroupa et al. (1993, Equation (14)).
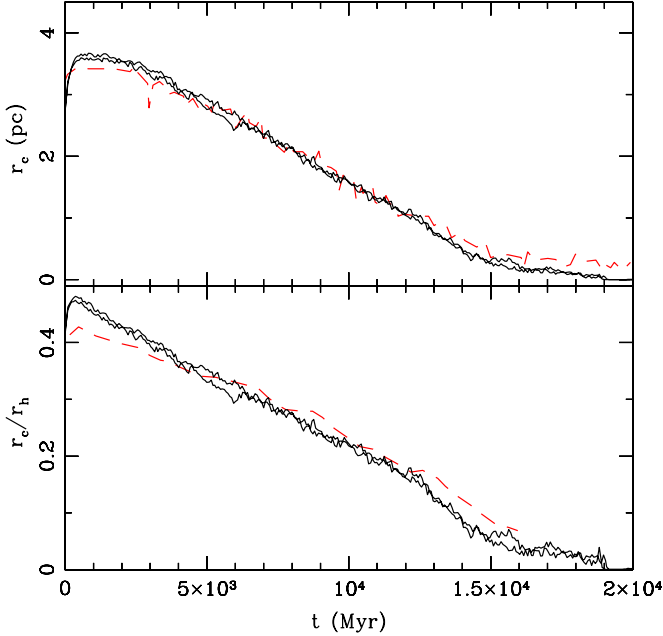
Figure 2. Evolution of r_c (top) and r_c/r_h (bottom). In each panel, the solid black lines show results from simulations using CMC. The two black lines show the results using two different realizations of the same initial cluster using two different initial seeds for model hcn1e5b5 (Table 1). The red dashed lines show results from Hurley07 for their K100-5 model. In the top and bottom panels, Hurley07 results are taken from Hurley et al. (2007) and Hurley (2007), respectively. Although they are from the same simulation (private communication), the results for r_c/r_h are not shown beyond 16 Gyr in Hurley (2007). All data from Hurley07 used for comparison in this work are extracted using ADS's Dexter data extraction applet (Demleitner et al. 2001).

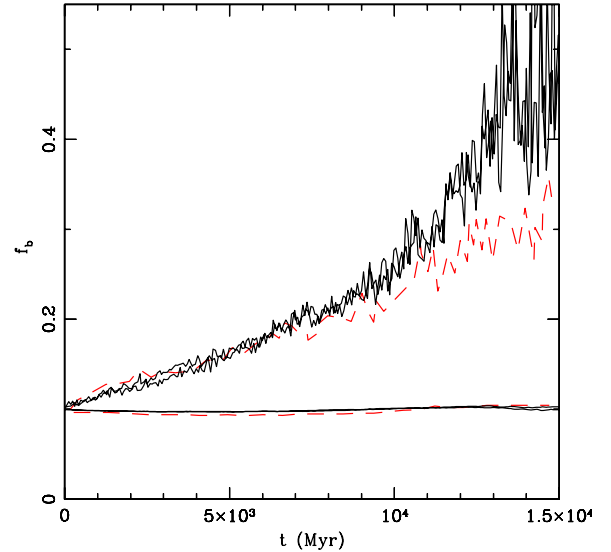(A color version of this figure is available in the online journal.)

the cluster reaches the binary-burning phase (e.g., Fregeau & Rasio 2007). All of these qualitatively different phases of the evolution of a cluster are reproduced using CMC with excellent agreement.

One of the key results of Hurley07 is that the overall binary fraction (f_b) remains close to the primordial value throughout the evolution of the cluster (also see Fregeau et al. 2009). This result has immense observational significance. In practice, only the present-day properties of a cluster are observed. This result from Hurley07 indicates that if a present-day binary fraction of the cluster close to r_h can be observed the primordial hard f_b should have been close to this observed value. Figure 3 shows the evolution of the core ($f_{b,c}$) and the overall f_b from CMC simulation hcn1e5b5 and direct N-body simulation presented in Hurley07. Binaries preferentially sink to the center due to mass segregation and the single stars typically get tidally disrupted from the tidal boundary. These two effects compete with each other—the first reduces and the second increases f_b outside the core. For the simulated cluster these two effects more or less balance each other. For the simulated cluster we reproduce the results presented in Hurley07 and verify that the overall f_b remains close to the primordial value whereas $f_{b,c}$ increases over
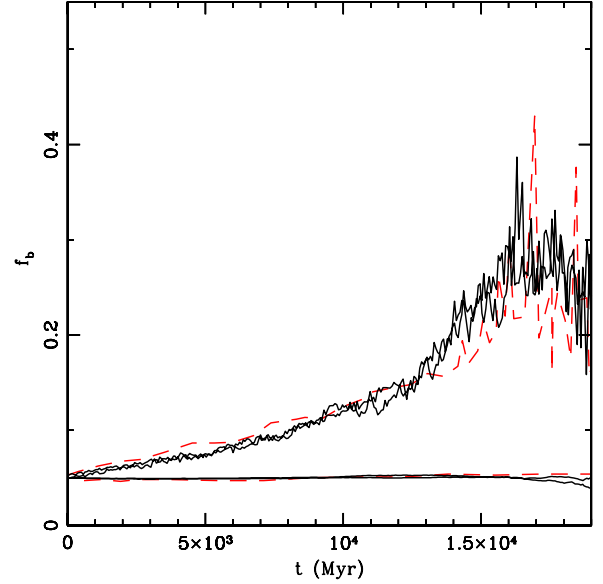
Figure 3. Comparison of evolution of the core and the overall binary fraction. Dashed red lines show results from Hurley et al. (2007, their K100-5 run). Solid black lines show results from CMC runs using two realizations of the model hcn1e5b5 (Table 1). In each set, the top line shows the binary fraction within the core and the bottom line shows that for the whole cluster.

(A color version of this figure is available in the online journal.)

Figure 4. Same as Figure 3, but using results from simulation hcn1e5b10. The CMC results are compared with the K100-10 simulation of Hurley07.

(A color version of this figure is available in the online journal.)

time. Similar results are found for the simulation hcn1e5b10 (Figure 4).

We now focus on the evolution of the number of binaries in the core ($N_{b,c}$). The evolution of the total number of core binaries is interesting for various reasons. The formation rates
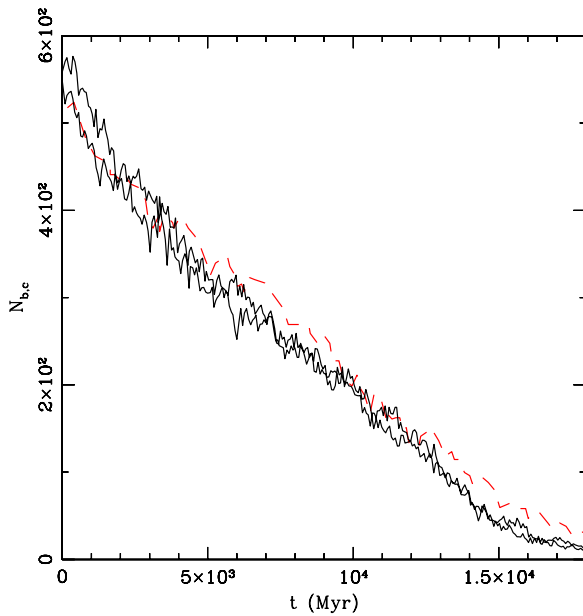
Figure 5. Evolution of number of binaries within r_c ($N_{b,c}$). The solid black lines show the results from CMC runs `hcn1e5b5` and the red dashed line shows results from direct N-body run K100-5 from Hurley07.

(A color version of this figure is available in the online journal.)

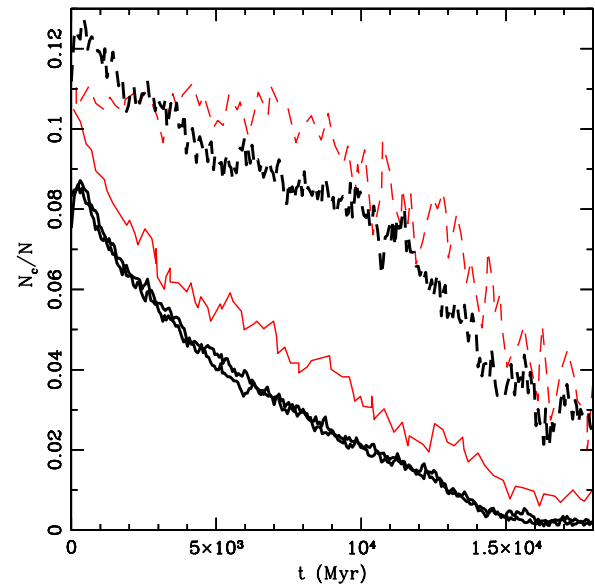**Figure 6.** Evolution of the fraction (by number) of binary and single stars within the core. Thick black lines show the results from CMC for model `hcn1e5b5` (Table 1). Thin red lines show the same from Hurley07 (their model K100-5). Solid and dashed lines show the number of singles and binaries within r_c, respectively. All numbers are normalized with the total number of that species at that time in the cluster (e.g., $N_{b,c}/N_b$ for the binaries). Both results clearly show the effects of mass segregation since throughout the evolution a higher fraction of binaries reside in the core.

(A color version of this figure is available in the online journal.)
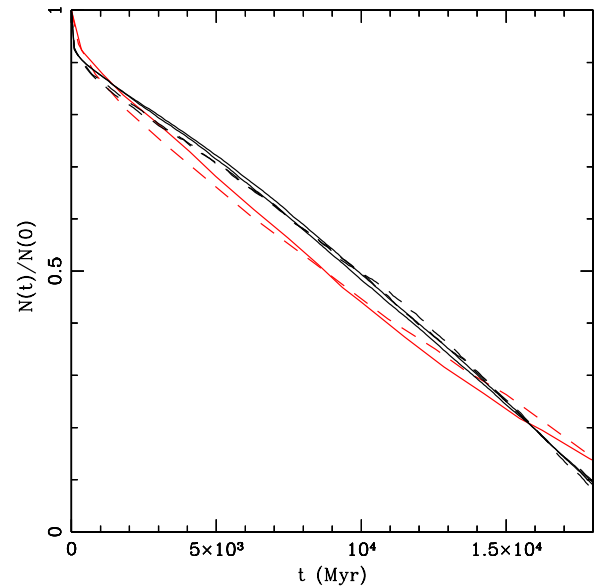
Figure 7. Comparison of the evolution of the number of single and binary stars that remain bound to the cluster. Red lines show results obtained from Hurley07 (their model K100-5). Black lines show results from CMC runs using two different realizations of model `hcn1e5b5` (Table 1). Solid lines for both cases show the number of single stars bound at any given time. Dashed lines show the same for binaries. All numbers are normalized to the initial number of the same species (single or binary).

(A color version of this figure is available in the online journal.)

of interesting stellar objects such as X-ray binaries and blue straggler stars and their properties are directly dependent on $N_{b,c}$, motivating many detailed studies focusing on its evolution (e.g., Hurley et al. 2002; Ivanova et al. 2005, 2006, 2008; Fregeau et al. 2009). On the one hand, the core binary number ($N_{b,c}$) increases due to mass segregation. On the other hand, strong interactions involving BS and BB encounters can lead to direct physical collisions or destruction of binaries and reduce $N_{b,c}$. In addition, binary stellar evolution can destroy binaries via evolution-driven mergers and disruptions. Since the evolution of $N_{b,c}$ is dependent on these competing effects, it is not simple to predict its evolution a priori. Figure 5 shows the evolution of the number of core binaries ($N_{b,c}$) for CMC run `hcn1e5b5` and direct N-body run K100-5 from Hurley07 for comparison. The evolution of $N_{b,c}$ is reproduced almost exactly within the numerical fluctuations of the simulations. Over time the number of core binaries ($N_{b,c}$) decreases.

It is also interesting to study the number fractions of binaries and single stars within the core compared to the global population. Although $N_{b,c}$ decreases over time, due to mass segregation effects the number single stars within r_c decreases more. Figure 6 shows the evolution of the number fractions of single stars ($n_{s,c}$) and binaries ($n_{b,c}$) within r_c for the same simulations as above. During the first $\sim 10^4$ Myr $n_{b,c}$ remains more or less constant whereas $n_{s,c}$ decreases by ~ 0.5 of the initial $n_{s,c}$ due to mass segregation effects. Followed by this phase, BS/BB interactions as well as stellar evolution destroy core binaries decreasing $n_{b,c}$. However, throughout the evolution $n_{b,c} > n_{s,c}$. The combined effects of the above lead to the overall increase in $f_{b,c}$ over time as seen in Figures 3 and 4. Note that although qualitatively CMC results and the direct N-body results agree, the agreement is not as excellent as the previous comparisons. For example, for the evolution of $n_{b,c}$ there can be up to $\approx 20\%$ difference in the absolute value depending on the age of the simulated cluster. The reason behind this larger difference compared with the excellent agreement for the evolution of $N_{b,c}$ (Figure 5) originates from the approximations adopted

in the tidal treatment in MC methods. The energy criterion (Equation (3); Giersz et al. 2008) based tidal removal of stars adopted in CMC loses stars from the tidal boundary at a relatively lower rate (Figure 7). Hence, at a given time the total number of bound single and binary stars in CMC are higher than those in Hurley07 making both $n_{b,c}$ and $n_{s,c}$ calculated
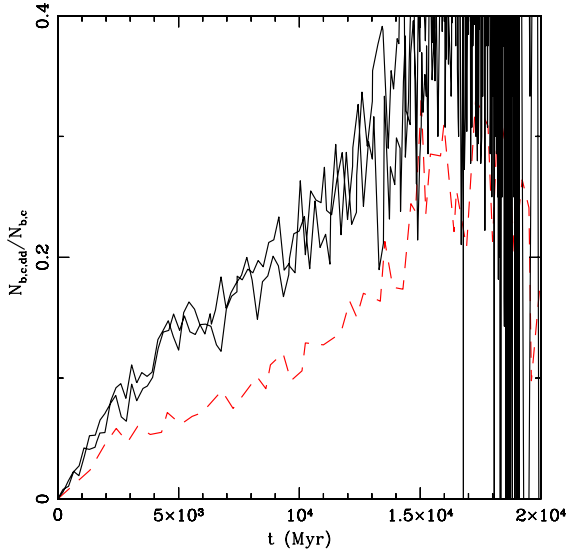
Figure 8. Evolution of the fraction of double-degenerate binaries within r_c with respect to all core binaries. Black solid and red dashed lines show results from CMC simulations (model `hcn1e5b5`, Table 1) and direct N-body simulation in Hurley07 (their model `K100-5`), respectively.

(A color version of this figure is available in the online journal.)

using CMC systematically lower than the same calculated in Hurley07.

Another interesting result presented in Hurley07 is the evolution of the fraction of binaries in the core where both components are compact objects. We call them double-degenerate binaries following Hurley07. In Figure 8, we show the evolution of the fraction of double-degenerate core binaries for CMC run `hcn1e5b5` and direct N-body run K100-5. The fraction of double-degenerate binaries in the core depends on all physical processes in the cluster in a complicated way. Two-body relaxation drives mass segregation in the cluster determining the densities at different radial regions of the cluster as well as radius-dependent velocity dispersion. This in turn directly affects the local BS/BB scattering cross section at a given time, consequently determining the survivability of a given binary at some radial position in the cluster, along with the properties of the binary. Changing the binary stellar and orbital properties in turn modifies the evolutionary pathways taken by the binary members and, consequently, compact object formation. Stellar evolution and dynamical effects thus in tandem affect the fraction of double-degenerate binaries in the core. The CMC results agree qualitatively with Hurley07 results indicating that not only the dynamical effects but also the stellar evolution and the rate of compact object formation are modeled reasonably accurately. Nevertheless, CMC simulations tend to overproduce the double degenerate binaries within the core compared to the Hurley07 simulations. Note that this result is subject to numerical fluctuations to a high degree since there are only a small number (e.g., 14 on an average for one realization of `hcne5b5`) of double degenerate binaries in the core throughout the evolution. This quantitative disagreement may also result if the version of BSE used in NBODY4 and thus in Hurley07 simulations and that integrated with CMC are not exactly the same.

4. COMPARISON WITH SIMULATIONS WITHOUT STELLAR EVOLUTION

We now examine the effects of stellar evolution on the evolution of the global observable properties of a GC, by performing

Table 2
Initial Conditions for Comparison Runs Including and Leaving Out Stellar Evolution

Name	N	Profile	IMF	f_b
kw4b03	10^5	King	K01 [0.1, 1.2] $M_\odot$	0.03
kw4b1	10^5	King	K01 [0.1, 1.2] $M_\odot$	0.1
kw4b3	10^5	King	K01 [0.1, 1.2] $M_\odot$	0.3
kw7b0	5×10^5	King	K01 [0.1, 18.5] $M_\odot$	0
kw7b1	5×10^5	King	K01 [0.1, 18.5] $M_\odot$	0.1

comparisons to simulations without stellar evolution. The initial conditions for these simulations are summarized in Table 2.

Our previous paper, Paper IV, showed results from simulations without stellar evolution, but all other physical processes were included. In the absence of an implementation of full single and binary stellar evolution, Paper IV restricted itself to simulations with a narrow range of masses in the IMF. We first compare the results with stellar evolution with a small subset of the previous runs from Paper IV without stellar evolution with the narrow IMF as an example. Since this is for the purpose of comparison, we use the apocenter criterion (Section 2) for the tidal treatment to be consistent with Paper IV for these simulations.

For each of these simulations, the initial stellar positions and velocities are chosen from a King profile with the concentration parameter $W_0 = 4$. For each simulation $N_i = 10^5$. The stellar IMF is chosen from the stellar MF presented in K01. The initial binary fraction is $f_b = 0.03, 0.1$, or 0.3. The mass of each binary companion is chosen in the range 0.1–m_p, where m_p is the mass of the primary, from a uniform distribution in mass ratios. The binary periods are chosen from a distribution flat in $\log a$ within physical limits, where the hardest binary has $a > 5 \times$ the sum of the stellar radii of the companions and the softest binary is at the local hard–soft boundary. Binary eccentricities are thermal (e.g., Heggie & Hut 2003). For each of these initial conditions, one simulation is done including stellar evolution and the other leaving it out.

We find that, even for the simulations with a small range of initial stellar masses, where the stellar evolution mass loss is not as severe as in a realistic cluster, for low f_b stellar evolution can influence the overall cluster evolution to a certain extent. Figure 9 shows the evolution of r_c/r_h. The results are shown for runs `kw4b0.03, 0.1, 0.3` (see Table 2). From top to bottom the primordial binary fractions f_b are 0.03, 0.1, 0.3, respectively. For $f_b = 0.03$ even with the narrow mass range, the two curves start diverging when the most massive stars (in this case $1.2 M_\odot$) evolve off their MS and lose mass via compact object formation after ≈ 3.4 Gyr.

Binary interactions take place throughout the evolution of the cluster. As the initial f_b is increased, energy available from super-elastic scattering of binaries becomes relatively more important compared to the energy produced from stellar evolution mass loss. Thus for this narrow range of masses, as the binary fraction is increased, the difference between the results from simulations including stellar evolution and results without including stellar evolution reduces. For example, evolution of the cluster with initial $f_b = 30\%$ is very similar with and without stellar evolution taken into account. The only difference is that at the quasi-steady binary-burning phase including stellar evolution makes r_c/r_h bigger by about 30%. In each of these clusters, the central densities are not very high ($\sim 10^4 M_\odot$ pc^{-3}) so direct SS collisions are not dominant. When direct SS
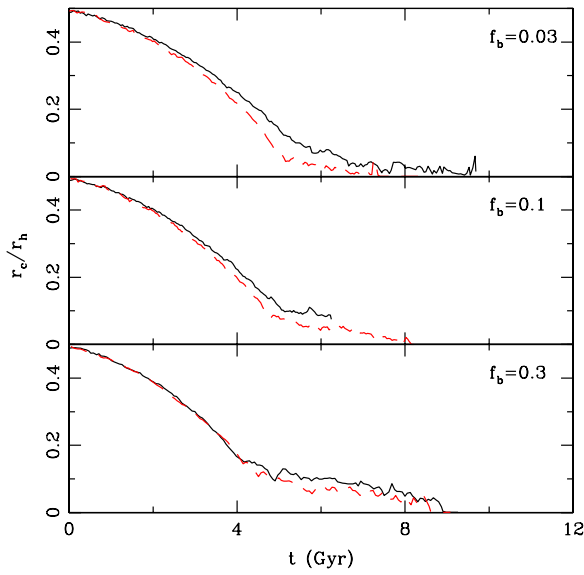
Figure 9. Comparison of the evolution of r_c/r_h with (solid black) and without (dashed red) stellar evolution, both using CMC. Results without stellar evolution were already presented in Paper IV. Each run starts with 10^5 objects. The velocities and positions of the objects are chosen from a King profile with an initial $W_0 = 4$. The masses are chosen from a Salpeter MF in the range 0.2–$1.2\,M_\odot$. From top to bottom, models kw4b03, kw4b1, and kw4b3 (Table 2) with initial binary fractions 0.03, 0.1, and 0.3, respectively, are shown.

(A color version of this figure is available in the online journal.)

collisions are more important in a much denser cluster, this behavior may change (Chatterjee et al. 2008).

The difference in the evolution of the global properties depending on whether stellar evolution was included or not is, of course, a lot more dramatic when a more realistic IMF with a wider mass range is used. Here we use a King profile with central concentration parameter $W_0 = 7$. The IMF is according to the K01 stellar MF in the range 0.1–$18.5\,M_\odot$. Two such clusters are simulated, one with no primordial binaries and the other with $f_b = 0.1$. Note the dramatic difference in the evolution of the simulated clusters in Figure 10. The evolution during the initial $\sim 10^2$ Myr is dominated by the mass loss via stellar evolution of the high-mass stars and compact object formation (Figure 11). This phase is clearly distinguished by the initial steep expansion of the cluster (Figure 10). Note that the initial steep expansion of r_c lags behind the initial peak in the mass-loss rate (Figures 10 and 11). This is because initially the cluster is not mass segregated and the high-mass stars are distributed throughout the cluster. The high-mass stars sink to the core at the mass segregation timescale (~ 0.1 Gyr at the r_h for model kw7b0). Mass loss due to stellar evolution becomes fully effective only after the high-mass stars sink to the core due to mass segregation. After this time, most of the mass is lost from inside the core resulting in a rapid expansion of r_c. Thus, the rapid core expansion lags behind the initial peak of the mass-loss rate by approximately the initial mass segregation timescale.

This phase is followed by a slow contraction phase. In this phase, two-body relaxation drives the evolution. The high-mass stars have already evolved off the MS and the stars remaining in the cluster are evolving at a much slower rate. The transition between the initial stellar evolution driven expansion and the slow contraction happens when the energy generation rate from stellar evolution mass loss becomes less than the outward energy diffusion rate from the core due to relaxation. The
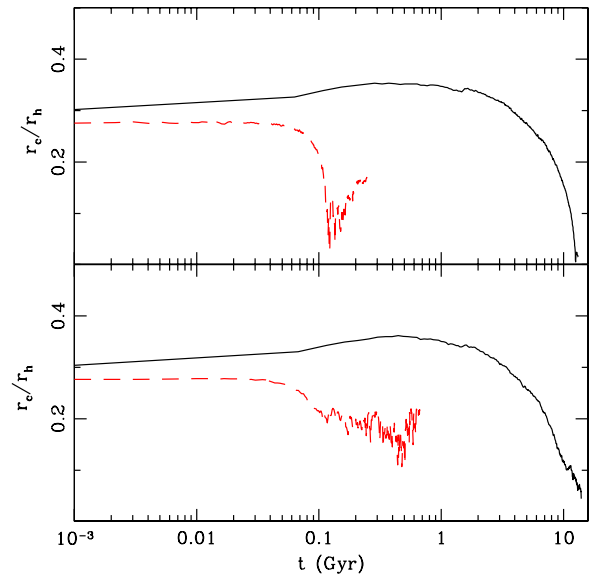
Figure 10. Comparison between two sets of simulations, all using CMC, but in one set stellar evolution is included and in the other it is not. Models kw7b0, 1 (Table 2) are used. Both panels show simulations with an initial King profile cluster with $W_0 = 7$ and a Kroupa (2001) IMF in the range 0.1–$18.5\,M_\odot$. The top panel shows results with no primordial binaries. The bottom panel shows results with 0.1 initial f_b. For all simulations the initial number of objects is 5×10^5. On both panels, dashed red lines are for simulations leaving out stellar evolution and solid black lines are for simulations including stellar evolution. A dramatic difference is clearly noticeable caused by stellar evolution mass loss. In each case, the simulations are stopped when either of the following is fulfilled: a deep collapse stage is reached, a binary burning stage is reached, or cluster is simulated for 12 Gyr.

(A color version of this figure is available in the online journal.)
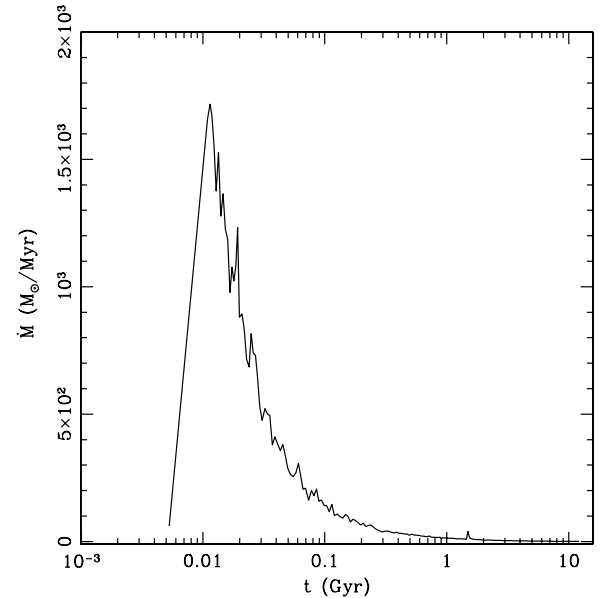
Figure 11. Rate of stellar evolution mass loss as a function of time for model kw7b0 (Table 2). Within 10–100 Myr most of the mass is lost due to stellar evolution, while high-mass stars $M_\star \gtrsim 5\,M_\odot$ evolve off their MS. Followed by this initial phase the mass-loss rate from winds and compact object formation is low.

cluster then keeps contracting until the central density increases so much that BS/BB interaction rates become high enough and the energy injected by the hard binaries (via super-elastic scattering) balances the energy diffusion rate from relaxation. The cluster then reaches the binary-burning phase (bottom panel of Figure 10).

Even with this moderately broad range of mass, the models without stellar evolution contract rapidly and are driven toward a quick collapse. If there are primordial binaries, the binary-burning phase starts relatively early ($\sim$1 Gyr, Figure 10). On the other hand, when stellar evolution is included, even without any primordial binaries the same cluster may still be in the slow contraction phase after a Hubble time. For the cluster with primordial binaries in this case the binary-burning starts only after 11 Gyr (Figure 10).

5. RESULTS FOR REALISTIC GALACTIC GLOBULAR CLUSTERS

We have validated CMC by extensive comparisons with direct N-body results (Section 3). Moreover, we have shown the importance of including stellar evolution in cluster modeling using a realistic stellar IMF (Section 4). We now simulate a large grid of clusters with realistic initial conditions for 12 Gyr taking all physical processes into account, including primordial binaries and single and binary stellar evolution, and the full observed stellar mass range spanning 3 orders of magnitude. Our goal here is to simulate clusters with realistic initial conditions motivated from observations of young clusters (e.g., Scheepmaker et al. 2007) and find whether at a simulated cluster age of $\approx$12 Gyr, a typical age for the GGCs, the simulated clusters show similar observable properties (e.g., r_c and r_c/r_h) as the observed population.

The proper initial conditions for the GGCs are uncertain, however. Moreover, it is hard to uniquely infer the initial conditions from the present-day observed cluster properties since the observed cluster global properties as well as their galactic orbits can be quite uncertain (e.g., Heggie & Giersz 2008). Hence, rather than trying to create a detailed model for any particular cluster we compare the collective results of all our grid runs with the observed GGC properties as a whole. The GGC properties are extracted from the Harris Catalog for GGCs (Harris 1996, and references therein; also see http://www.physics.mcmaster.ca/Globular.html). When an observable is not reported in the catalog for a cluster, we exclude that cluster from comparison. In the following subsections, we explain the initial setup of the grid of simulations and present our results.

5.1. Initial Conditions

We simulate clusters with a large grid of initial conditions. All simulated clusters have a fixed initial virial radius $r_v = 4$ pc (corresponds to an initial $r_h \approx 3$ pc). Indeed, observations indicate that the effective radii of both young and old clusters are rather insensitive to the cluster mass, and metallicity (e.g., Ashman & Zepf 2001; Scheepmaker et al. 2007, 2009) and have a median value of $\sim$3 pc. In addition, observations of old massive LMC clusters, old GCs in NGC 5128, old clusters in M 51, as well as the GGCs indicate that the effective cluster radii show only a weak correlation with the distance from the galactic center (Hodge 1962; Harris et al. 1984; Hesser et al. 1984; Mateo 1987; van den Bergh et al. 1991; Scheepmaker et al. 2007; Hwang & Lee 2008).

To restrict the huge parameter space to a certain extent we place all our simulated clusters in a circular orbit at a Galactocentric distance of $r_G = 8.5$ kpc, where the Galactic field is not so strong that the tidal stellar loss dominates the cluster's evolution. Choosing a circular orbit for the simulated clusters is a simplification; however, the results should still be valid for eccentric orbits with some effective Galactocentric distance (>8.5 kpc; e.g., Baumgardt & Makino 2003). The Galactic tidal field and consequently the initial r_t for the clusters are calculated using a Galactic rotation speed $v_G = 220\,\mathrm{km\,s^{-1}}$ following Equation (5).

For the set of runs we vary N_i between 4 and 10×10^5, the initial W_0 for King models in the range 4–7.5, and initial f_b between 0 and 0.1. For each case we choose the stellar masses of the primaries from the MF presented in K01 in the range 0.1–$100\,M_\odot$. The mass of each binary companion is chosen from a uniform distribution of mass ratios in the range $0.1\,M_\odot$–m_p. a is chosen from a distribution flat in log within physical limits, namely, $5\times$ the physical contact of the components and the local hard–soft boundary. Although initially each binary is hard at its position it may not remain so during the evolution of the cluster. The cluster contracts under two-body relaxation and the velocity dispersion increases making initially hard binaries soft. Moreover, binaries sink to the core due to mass segregation where the velocity dispersion is higher than the velocity dispersion for the binaries at $t = 0$. We include these soft binaries in our simulations. We let the cluster dynamics disrupt these binaries via BS/BB interactions. So at any instant of time soft binaries are allowed in the cluster as long as they have not been disrupted naturally via dynamical encounters yet. This is closer to reality and this strategy is adopted because soft binaries can act as an energy sink and can contribute to the overall cluster energetics significantly (Fregeau et al. 2009).

Each cluster is evolved for 12 Gyr including all physical processes—two-body relaxation, stellar evolution, and strong encounters such as BB, BS, and SS collisions. For clusters that reach a deep-collapse phase, the CMC time steps become minuscule and the code grinds to a halt. We stop our simulations at that point for these clusters. Note that in reality, the deep collapse phase is halted via formation of the so-called three-body binaries and the cluster enters into the gravothermal oscillation phase. Since in CMC we do not include the possibility of creating new binaries via three body encounters, we do not address this phase at this stage. However, this is not a serious limitation for this study since all simulated clusters that reach this phase within 12 Gyr had a primordial $f_b = 0$, which is not realistic (e.g., see most recently Davis et al. 2008) and simulated as limiting cases. None of the simulated clusters enter into the deep-collapse phase before $\approx$9 Gyr. The properties of all simulated clusters are summarized in Table 3. We use $\gamma = 0.01$ in the Coulomb logarithm for these simulations.

5.2. Results

Here, we present some basic observable properties of the simulated clusters and compare them with the same properties of the observed GGCs. For each of these comparison plots, the evolution of a cluster property is shown with the distribution of the same property in the GGC population including all GGCs where observation of the concerned property exists. Since we restrict the galactocentric distance of our simulated clusters for this study to be 8.5 kpc (Section 5.1) we also show the observed distribution for the GGCs with pericenter distances from the Galactic center within 7–10 kpc to be consistent in the comparisons. Note that the purpose for this comparison is simply to ensure that the simulated cluster properties agree well with the observed GGC properties. We do not intend to create a present-day distribution for these properties since for that a probability distribution for the initial conditions is required, which is poorly constrained and beyond the scope of this study.

Table 3
List of Simulations

Name	Initial									Final										
	W_0	M	N	r_c	r_h	ρ_c	f_b	$f_{b,c}$	c	t	M	N	r_c	$r_{c,\text{obs}}$	r_h	ρ_c	f_b	$f_{b,c}$	c	c_{obs}
c1f1n1	4	2.5	4	1.6	3.3	12.2	0.00	0.00	1.1	12	1.4	3	2.0	2.1	7.1	1.0	0.00	0.00	1.5	1.5
c1f1n2	4	3.8	6	1.6	3.3	16.2	0.00	0.00	1.5	12	2.1	5	2.3	2.2	7.0	1.1	0.00	0.00	1.5	1.5
c1f1n3	4	5.1	8	1.6	3.3	23.3	0.00	0.00	1.7	12	2.8	7	2.4	2.1	6.9	1.2	0.00	0.00	1.5	1.5
c1f1n4	4	6.4	10	1.6	3.3	29.0	0.00	0.00	1.6	12	3.5	9	2.5	2.0	6.8	1.4	0.00	0.00	1.5	1.6
c1f2n1	4	2.6	4	1.6	3.3	12.3	0.05	0.05	1.3	12	1.4	3	2.1	2.3	7.2	0.9	0.05	0.07	1.4	1.5
c1f2n2	4	3.9	6	1.6	3.3	17.3	0.05	0.05	1.6	12	2.1	5	2.3	2.2	7.1	1.1	0.05	0.07	1.5	1.5
c1f2n3	4	5.3	8	1.6	3.3	24.7	0.05	0.05	1.7	12	2.9	7	2.5	2.2	7.0	1.2	0.05	0.07	1.5	1.5
c1f2n4	4	6.6	10	1.6	3.3	30.2	0.05	0.05	1.7	12	3.6	9	2.5	2.0	6.9	1.4	0.05	0.06	1.5	1.6
c1f3n1	4	2.7	4	1.6	3.3	12.4	0.10	0.10	1.2	12	1.4	3	2.1	2.3	7.3	0.9	0.09	0.14	1.4	1.5
c1f3n2	4	4.0	6	1.6	3.3	17.7	0.10	0.10	1.3	12	2.2	5	2.3	2.2	7.2	1.1	0.09	0.14	1.5	1.5
c1f3n3	4	5.4	8	1.6	3.3	25.3	0.10	0.10	1.5	12	2.9	7	2.5	2.2	7.1	1.2	0.09	0.13	1.5	1.5
c1f3n4	4	6.8	10	1.6	3.3	30.9	0.10	0.10	1.7	12	3.7	9	2.6	2.1	7.0	1.4	0.09	0.12	1.5	1.5
c2f1n1	4.5	2.5	4	1.5	3.3	14.2	0.00	0.00	1.0	12	1.4	3	1.9	2.0	7.1	1.3	0.00	0.00	1.5	1.5
c2f1n2	4.5	3.8	6	1.5	3.3	18.8	0.00	0.00	1.5	12	2.1	5	2.1	2.0	7.0	1.4	0.00	0.00	1.5	1.5
c2f1n3	4.5	5.1	8	1.5	3.3	27.2	0.00	0.00	1.4	12	2.8	7	2.3	2.0	6.9	1.5	0.00	0.00	1.5	1.6
c2f1n4	4.5	6.4	10	1.5	3.3	33.3	0.00	0.00	1.4	12	3.5	9	2.3	2.0	6.9	1.7	0.00	0.00	1.5	1.6
c2f2n1	4.5	2.6	4	1.5	3.3	14.3	0.05	0.05	1.0	12	1.4	3	1.9	2.1	7.3	1.2	0.05	0.07	1.5	1.5
c2f2n2	4.5	3.9	6	1.5	3.3	20.1	0.05	0.05	1.7	12	2.1	5	2.2	2.1	7.2	1.3	0.05	0.07	1.5	1.5
c2f2n3	4.5	5.3	8	1.5	3.3	28.9	0.05	0.05	1.6	12	2.8	7	2.3	2.1	7.1	1.4	0.05	0.07	1.5	1.5
c2f2n4	4.5	6.6	10	1.5	3.3	34.7	0.05	0.05	1.7	12	3.6	9	2.4	2.0	7.0	1.7	0.05	0.07	1.5	1.6
c2f3n1	4.5	2.7	4	1.5	3.3	14.4	0.10	0.10	1.0	12	1.4	3	2.0	2.2	7.4	1.2	0.09	0.14	1.5	1.5
c2f3n2	4.5	4.0	6	1.5	3.3	20.5	0.10	0.10	1.8	12	2.2	5	2.2	2.1	7.3	1.3	0.09	0.14	1.5	1.5
c2f3n3	4.5	5.4	8	1.5	3.3	29.6	0.10	0.10	1.4	12	2.9	7	2.4	2.1	7.2	1.3	0.09	0.13	1.5	1.5
c2f3n4	4.5	6.8	10	1.5	3.3	35.4	0.10	0.10	1.4	12	3.7	9	2.4	2.0	7.1	1.7	0.09	0.13	1.5	1.6
c3f1n1	5	2.5	4	1.4	3.2	17.2	0.00	0.00	1.2	12	1.4	3	1.7	1.9	7.3	1.7	0.00	0.00	1.5	1.5
c3f1n2	5	3.8	6	1.4	3.3	22.4	0.00	0.00	1.4	12	2.1	5	2.0	2.0	7.1	1.7	0.00	0.00	1.5	1.6
c3f1n3	5	5.1	8	1.4	3.3	32.5	0.00	0.00	1.7	12	2.8	7	2.1	2.0	7.0	1.9	0.00	0.00	1.6	1.6
c3f1n4	5	6.4	10	1.4	3.3	40.0	0.00	0.00	1.6	12	3.5	9	2.2	2.0	7.0	2.1	0.00	0.00	1.6	1.6
c3f2n1	5	2.6	4	1.4	3.2	17.3	0.05	0.05	1.3	12	1.4	3	1.7	2.1	7.4	1.7	0.05	0.08	1.5	1.5
c3f2n2	5	3.9	6	1.4	3.3	24.0	0.05	0.05	1.3	12	2.1	5	2.0	2.0	7.3	1.6	0.05	0.07	1.5	1.5
c3f2n3	5	5.3	8	1.4	3.3	34.6	0.05	0.05	1.5	12	2.8	7	2.2	2.0	7.2	1.8	0.05	0.07	1.5	1.6
c3f2n4	5	6.6	10	1.4	3.3	41.6	0.05	0.05	1.7	12	3.6	9	2.2	2.0	7.1	2.0	0.05	0.07	1.5	1.6
c3f3n1	5	2.7	4	1.4	3.2	17.4	0.10	0.10	1.5	12	1.4	3	1.8	2.1	7.6	1.5	0.09	0.15	1.5	1.5
c3f3n2	5	4.0	6	1.4	3.3	24.5	0.10	0.10	1.5	12	2.2	5	2.0	2.1	7.4	1.6	0.09	0.14	1.5	1.5
c3f3n3	5	5.4	8	1.4	3.3	35.4	0.10	0.10	1.4	12	2.9	7	2.2	2.1	7.3	1.8	0.09	0.13	1.5	1.6
c3f3n4	5	6.8	10	1.4	3.3	42.5	0.10	0.10	1.5	12	3.6	9	2.3	2.0	7.2	2.0	0.09	0.13	1.5	1.6
c4f1n1	5.5	2.5	4	1.3	3.2	21.6	0.00	0.00	1.2	12	1.4	3	1.5	1.8	7.4	2.5	0.00	0.00	1.6	1.6
c4f1n2	5.5	3.8	6	1.3	3.2	27.6	0.00	0.00	1.7	12	2.1	5	1.8	1.9	7.3	2.4	0.00	0.00	1.6	1.6
c4f1n3	5.5	5.1	8	1.3	3.3	40.2	0.00	0.00	1.4	12	2.8	7	1.8	2.0	7.2	2.9	0.00	0.00	1.6	1.6
c4f1n4	5.5	6.4	10	1.3	3.2	49.6	0.00	0.00	1.8	12	3.5	9	2.0	2.0	7.1	2.9	0.00	0.00	1.6	1.6
c4f2n1	5.5	2.6	4	1.3	3.2	21.7	0.05	0.05	1.6	12	1.4	3	1.6	1.9	7.6	2.1	0.05	0.08	1.5	1.6
c4f2n2	5.5	3.9	6	1.3	3.2	29.7	0.05	0.05	1.3	12	2.1	5	1.8	1.9	7.4	2.4	0.05	0.08	1.6	1.6
c4f2n3	5.5	5.3	8	1.3	3.3	43.0	0.05	0.05	1.6	12	2.8	7	1.9	2.0	7.3	2.6	0.05	0.08	1.6	1.6
c4f2n4	5.5	6.6	10	1.3	3.2	51.5	0.05	0.05	1.8	12	3.6	9	2.0	2.0	7.2	2.8	0.05	0.07	1.6	1.6
c4f3n1	5.5	2.7	4	1.3	3.2	21.7	0.10	0.10	1.3	12	1.4	3	1.6	1.9	7.7	2.0	0.09	0.15	1.5	1.6
c4f3n2	5.5	4.0	6	1.3	3.2	30.3	0.10	0.10	1.3	12	2.2	5	1.9	1.9	7.5	2.3	0.09	0.15	1.6	1.6
c4f3n3	5.5	5.4	8	1.3	3.3	44.0	0.10	0.10	1.3	12	2.9	7	2.0	2.0	7.4	2.5	0.09	0.14	1.6	1.6
c4f3n4	5.5	6.8	10	1.3	3.2	52.5	0.10	0.10	1.8	12	3.6	9	2.1	2.0	7.3	2.6	0.09	0.13	1.6	1.6
c5f1n1	6	2.5	4	1.2	3.2	28.5	0.00	0.00	1.4	12	1.4	3	1.2	1.4	7.6	4.9	0.00	0.00	1.7	1.7
c5f1n2	6	3.8	6	1.2	3.2	35.7	0.00	0.00	1.3	12	2.1	5	1.4	1.4	7.5	4.7	0.00	0.00	1.7	1.8
c5f1n3	6	5.1	8	1.2	3.2	52.8	0.00	0.00	1.4	12	2.8	7	1.6	1.9	7.4	4.5	0.00	0.00	1.7	1.6
c5f1n4	6	6.4	10	1.2	3.2	64.3	0.00	0.00	1.7	12	3.5	9	1.7	2.0	7.3	4.9	0.00	0.00	1.7	1.6
c5f2n1	6	2.6	4	1.2	3.2	28.6	0.05	0.05	1.4	12	1.4	3	1.3	1.4	7.8	3.8	0.05	0.09	1.6	1.7
c5f2n2	6	3.9	6	1.2	3.2	38.5	0.05	0.05	1.3	12	2.1	5	1.5	1.9	7.7	4.1	0.05	0.08	1.6	1.6
c5f2n3	6	5.3	8	1.2	3.2	56.6	0.05	0.05	1.3	12	2.8	7	1.7	2.0	7.5	4.0	0.05	0.08	1.6	1.6
c5f2n4	6	6.6	10	1.2	3.2	66.5	0.05	0.05	1.7	12	3.6	9	1.8	2.0	7.4	4.3	0.05	0.07	1.6	1.6
c5f3n1	6	2.7	4	1.2	3.2	28.6	0.10	0.10	1.5	12	1.4	3	1.4	1.7	8.0	3.5	0.09	0.16	1.6	1.7
c5f3n2	6	4.0	6	1.2	3.2	39.3	0.10	0.10	1.3	12	2.2	5	1.6	1.9	7.8	3.8	0.09	0.16	1.6	1.6
c5f3n3	6	5.4	8	1.2	3.2	57.9	0.10	0.10	1.4	12	2.9	7	1.7	2.0	7.6	3.9	0.09	0.14	1.6	1.6
c5f3n4	6	6.8	10	1.2	3.2	67.9	0.10	0.10	1.8	7	3.8	9	2.3	1.9	6.9	1.9	0.09	0.13	1.5	1.6
c6f1n1	6.5	2.5	4	1.1	3.2	40.1	0.00	0.00	1.3	12	1.4	3	0.6	0.6	8.0	47.6	0.00	0.00	2.0	2.1
c6f1n2	6.5	3.8	6	1.1	3.2	49.3	0.00	0.00	1.4	12	2.1	5	1.1	1.2	7.7	9.7	0.00	0.00	1.8	1.8
c6f1n3	6.5	5.1	8	1.1	3.2	73.0	0.00	0.00	1.7	12	2.8	7	1.2	1.3	7.6	11.6	0.00	0.00	1.8	1.8
c6f1n4	6.5	6.4	10	1.1	3.2	88.8	0.00	0.00	1.6	12	3.5	9	1.3	1.3	7.5	9.4	0.00	0.00	1.8	1.8
c6f2n1	6.5	2.6	4	1.1	3.2	40.3	0.05	0.05	1.5	12	1.4	3	0.7	1.0	8.1	25.6	0.05	0.11	1.9	1.9

Table 3
(Continued)

| Name	Initial									Final									
	W_0	M	N	r_c	r_h	ρ_c	f_b	$f_{b,c}$	c	t	M	N	r_c	$r_{c,\mathrm{obs}}$	r_h	ρ_c	f_b	$f_{b,c}$	c	c_{obs}
c6f2n2	6.5	3.9	6	1.1	3.2	53.4	0.05	0.05	1.4	12	2.1	5	1.1	1.3	7.9	9.6	0.05	0.09	1.7	1.8
c6f2n3	6.5	5.3	8	1.1	3.2	78.5	0.05	0.05	1.7	12	2.8	7	1.3	1.4	7.8	8.1	0.05	0.08	1.7	1.8
c6f2n4	6.5	6.6	10	1.1	3.2	91.7	0.05	0.05	1.6	12	3.6	9	1.4	1.4	7.7	8.7	0.05	0.08	1.7	1.8
c6f3n1	6.5	2.7	4	1.1	3.2	40.2	0.10	0.10	1.4	12	1.4	3	1.0	1.3	8.2	11.2	0.09	0.18	1.8	1.8
c6f3n2	6.5	4.0	6	1.1	3.2	54.4	0.10	0.10	1.4	12	2.2	5	1.2	1.5	8.0	8.3	0.09	0.16	1.7	1.8
c6f3n3	6.5	5.4	8	1.1	3.2	80.2	0.10	0.10	1.4	12	2.9	7	1.4	1.5	7.9	8.1	0.09	0.15	1.7	1.8
c6f3n4	6.5	6.8	10	1.1	3.2	93.6	0.10	0.10	1.6	12	3.6	9	1.4	1.4	7.8	9.4	0.09	0.15	1.7	1.8
c7f1n1	7	2.5	4	0.9	3.2	61.0	0.00	0.00	1.5	11	1.4	3	0.3	1.3	8.2	241.9	0.00	0.00	2.3	1.8
c7f1n2	7	3.8	6	0.9	3.3	73.4	0.00	0.00	1.5	12	2.1	5	0.3	1.0	8.2	314.0	0.00	0.00	2.3	1.9
c7f1n3	7	5.1	8	0.9	3.3	110.3	0.00	0.00	1.5	12	2.8	7	0.7	0.8	8.0	56.3	0.00	0.00	2.0	2.1
c7f1n4	7	6.4	10	0.9	3.3	134.5	0.00	0.00	1.6	12	3.5	9	0.8	0.8	7.9	54.2	0.00	0.00	2.0	2.1
c7f2n1	7	2.6	4	0.9	3.2	61.1	0.05	0.05	1.5	12	1.4	3	0.8	0.8	8.5	19.3	0.05	0.11	1.8	2.0
c7f2n2	7	3.9	6	0.9	3.3	79.7	0.05	0.05	1.9	12	2.1	5	0.7	0.9	8.3	43.3	0.05	0.11	1.9	2.0
c7f2n3	7	5.3	8	0.9	3.3	118.9	0.05	0.05	1.5	12	2.8	7	0.9	1.1	8.2	29.5	0.05	0.10	1.9	1.9
c7f2n4	7	6.6	10	0.9	3.3	138.3	0.05	0.05	1.6	12	3.6	9	0.8	0.8	8.0	48.4	0.04	0.09	2.0	2.1
c7f3n1	7	2.7	4	0.9	3.2	60.8	0.10	0.10	1.7	12	1.4	3	0.9	1.1	8.6	17.4	0.09	0.19	1.8	1.8
c7f3n2	7	4.0	6	0.9	3.3	81.2	0.10	0.10	1.6	12	2.2	5	0.8	1.0	8.5	30.1	0.09	0.19	1.9	2.0
c7f3n3	7	5.4	8	0.9	3.3	121.3	0.10	0.10	1.5	12	2.9	7	1.1	1.2	8.2	15.9	0.09	0.17	1.8	1.8
c7f3n4	7	6.8	10	0.9	3.3	141.0	0.10	0.10	1.9	12	3.6	9	1.0	1.2	8.1	25.5	0.09	0.16	1.9	1.8
c8f1n1	7.5	2.5	4	0.7	3.3	103.6	0.00	0.00	1.6	9	1.4	3	0.3	0.4	8.4	267.0	0.00	0.00	2.3	2.3
c8f1n2	7.5	3.8	6	0.7	3.4	119.9	0.00	0.00	1.6	10	2.1	5	0.4	1.2	8.2	256.0	0.00	0.00	2.2	1.8
c8f1n3	7.5	5.1	8	0.7	3.4	181.1	0.00	0.00	1.6	10	2.8	7	0.4	1.0	8.2	275.1	0.00	0.00	2.2	1.9
c8f1n4	7.5	6.4	10	0.7	3.4	220.4	0.00	0.00	2.1	10	3.5	9	0.5	0.7	8.1	179.4	0.00	0.00	2.2	2.1
c8f2n1	7.5	2.6	4	0.7	3.3	103.6	0.05	0.05	1.6	12	1.4	3	0.7	0.9	8.9	27.0	0.05	0.11	1.9	2.0
c8f2n2	7.5	3.9	6	0.7	3.4	130.7	0.05	0.05	1.6	10	2.1	5	0.7	1.4	8.5	51.9	0.05	0.11	2.0	1.8
c8f2n3	7.5	5.3	8	0.7	3.4	195.8	0.05	0.05	1.6	10	2.8	7	0.8	1.2	8.3	44.3	0.05	0.10	1.9	1.8
c8f2n4	7.5	6.6	10	0.7	3.4	225.8	0.05	0.05	1.7	10	3.6	9	0.8	1.1	8.2	59.5	0.05	0.10	2.0	1.9
c8f3n1	7.5	2.7	4	0.7	3.3	103.0	0.10	0.10	1.6	11	1.4	3	0.9	1.3	8.9	18.4	0.09	0.20	1.8	1.8
c8f3n2	7.5	4.0	6	0.7	3.3	133.1	0.10	0.10	2.1	10	2.2	5	0.8	1.4	8.6	33.2	0.09	0.19	1.9	1.8
c8f3n3	7.5	5.4	8	0.7	3.4	199.3	0.10	0.10	1.6	10	2.9	7	0.9	1.3	8.4	40.9	0.09	0.18	1.9	1.8
c8f3n4	7.5	6.8	10	0.7	3.4	230.1	0.10	0.10	1.7	10	3.7	9	0.9	1.1	8.2	42.5	0.09	0.17	1.9	1.9

Notes. W_0 is the central concentration parameter for a King Profile (King 1966), Cluster mass M is in $10^5 \, M_\odot$, number of bound cluster objects N is given in 10^5, central Stellar mass density ρ_c is in $10^3 \, M_\odot \, \mathrm{pc}^{-3}$, r_c and r_h are in pc, time of final snapshot t is in Gyr, and c is the concentration parameter defined as $\log_{10}(r_t/r_c)$. All final values are extracted from the final snapshot of the simulated clusters. $r_{c,\mathrm{obs}}$ and c_{obs} are estimated from a single-mass best-fit King model to the 2D number density at the final snapshot of the cluster.

Figures 12 and 13 show the evolution of r_c and r_c/r_h, respectively. Both the r_c and r_c/r_h values of the simulated clusters agree well with the observed values in the GGC population, producing values at 12 Gyr close to the peak of the observed distribution. We should remind the readers, however, that these r_c and r_h values are not exactly the quantities observed directly. As mentioned before, r_c is the density-weighted core radius (Casertano & Hut 1985), related to a virial radius in the core, commonly used in N-body simulations, and can differ from an observed r_c by a factor of a few (Hurley 2007). Similarly, only the half-light radius is observed which may differ from the half-mass radius of a cluster. For example, for a typical simulated cluster c1f3n4 the half-light radius including all stars is 4.7 pc. If a luminosity cutoff of $L_\star < 20 \, L_\odot$ is used to exclude the brightest giants (a common practice for observers, e.g., Noyola & Gebhardt 2006) for the same cluster the half-light radius is 4.1 pc. The theoretically calculated half-*mass* radius for the same cluster at the same age is 7 pc.

Nevertheless, one should remember that without including stellar evolution the simulated r_c/r_h values resulting from binary burning were found to be about an order of magnitude smaller than in the observed population (e.g., Paper IV; Vesperini & Chernoff 1994) and several studies proposed different additional energy generation mechanisms to explain the large observed

r_c/r_h values (e.g., Trenti et al. 2007a; Chatterjee et al. 2008; Fregeau 2008; Mackey et al. 2008). It is thus pleasing to find such an agreement simply by including stellar evolution in the simulations and assuming that the initial typical cluster r_h is ∼few pc independent of the cluster mass and Galactocentric position (e.g., Scheepmaker et al. 2007, 2009), without the need for fine tuning of initial conditions or invoking exotic scenarios.

To focus on the distinct evolutionary stages of the clusters we now choose three models from our large grid of simulations. These models are representative of clusters in three distinct end stages. Cluster c1f3n4 is in the slow contraction phase at the integration stopping time and cluster age $t_{cl} = 12$ Gyr. Cluster c3f2n1 completes the slow contraction phase at $t_{cl} \sim 10$ Gyr, reaches the binary-burning quasi-steady phase, and remains in the binary-burning phase until the integration stopping time $t_{cl} = 12$ Gyr. Cluster c8f1n1 reaches the deep collapse phase at $t_{cl} \approx 9$ Gyr (Figure 14). Integration is stopped after this stage is reached. As mentioned earlier, cluster c8f1n1 has no primordial binaries and is shown only as a limiting case for comparison. All simulated clusters first expand due to stellar evolution mass loss during the first ∼1 Gyr. Followed by this initial expansion, the clusters slowly contract due to two-body relaxation. This slow contraction phase ends in the quasi-steady binary-burning phase for clusters with primordial binaries (Table 3, runs except
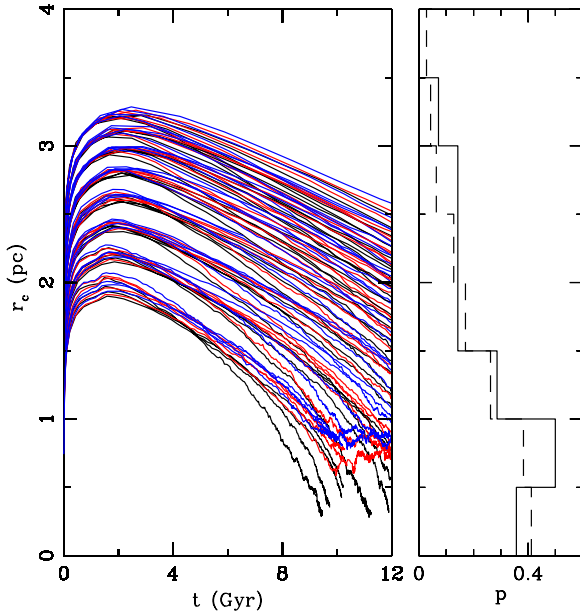
Figure 12. Evolution of r_c for all simulated clusters. The black, red, and blue lines are for clusters with initial $f_b = 0$, 0.05, and 0.1, respectively. A few (six) clusters with $f_b = 0$ go into deep collapse within a Hubble time. We stop integrations for those clusters when this phase is reached. The r_c values for the observed GGCs are also shown in histograms. The solid histogram is for GGCs with Galactocentric distances between 7 and 10 kpc. The dashed histogram is for all GGCs where a measurement for r_c exists.

(A color version of this figure is available in the online journal.)
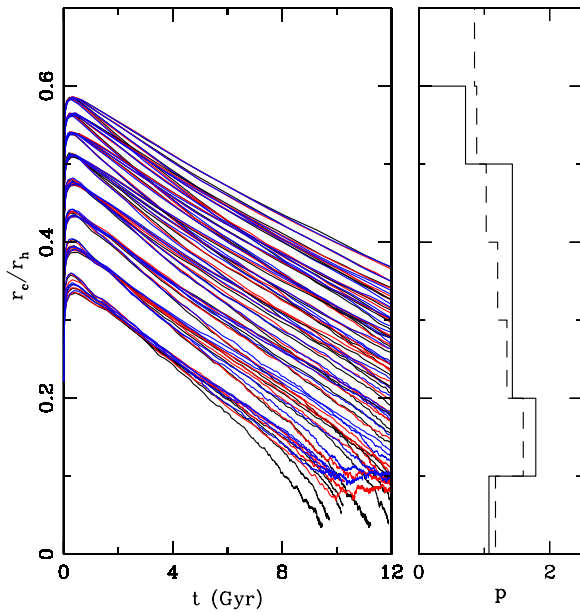
Figure 13. Same as Figure 12, but for r_c/r_h for all simulated clusters. The r_c/r_h values for the observed GGCs are also shown in histograms. The solid and dashed histograms are for GGCs selected as in Figure 12.

(A color version of this figure is available in the online journal.)

Figure 14. Evolution of r_c/r_h (top), r_c (middle), and r_h (bottom) for three qualitatively different clusters. Results from runs c1f3n4, c3f2n1, and c8f1n1 are shown in all three panels with solid, short-dashed, and long-dashed lines, respectively. Runs c1f3n4, c3f2n1, and c8f1n1 at their final stage of simulation are in the slow contraction, binary-burning, and deep-collapse phase, respectively.

(A color version of this figure is available in the online journal.)
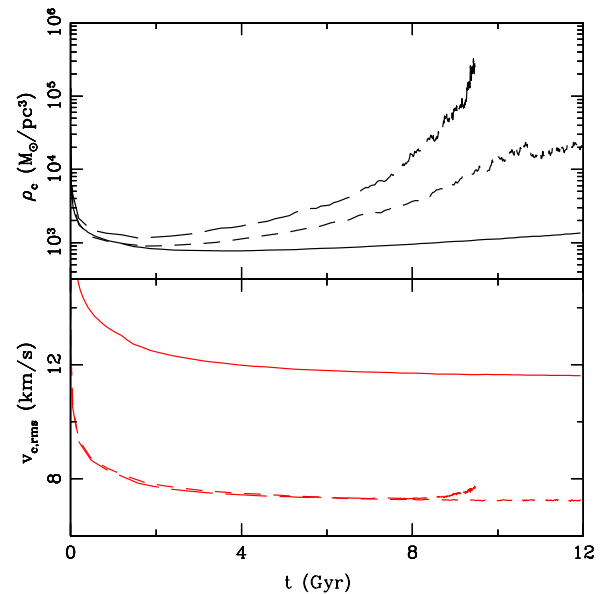
Figure 15. Evolution of the central stellar mass density (ρ_c, top) and the central rms velocity ($v_{c,\mathrm{rms}}$, bottom) for three example runs: c1f3n4 (solid), c3f2n1 (short-dashed), and c8f1n1 (long-dashed). ρ_c and $v_{c,\mathrm{rms}}$ decrease sharply during the initial stellar evolution driven expansion of the clusters. ρ_c increases slowly during the slow-contraction phase. In the binary-burning phase, ρ_c attains a quasi-steady value. A sharp increase in ρ_c is observed at the deep-collapse phase. $v_{c,\mathrm{rms}}$ remains more or less steady following the initial decrease. During deep-collapse $v_{c,\mathrm{rms}}$ rises.

(A color version of this figure is available in the online journal.)

cxf1nx). Clusters without primordial binaries go into deep collapse directly at the end of slow contraction.

The central density for each simulated cluster first decreases sharply during the initial stellar evolution dominated phase due to the early expansion of the core. During the slow contraction phase the cluster stellar density increases steadily and reaches a quasi-steady value during the binary-burning phase (Figure 15).

The central velocity dispersion ($v_{c,\mathrm{rms}}$) decreases sharply during the stellar evolution dominated phase. After that $v_{c,\mathrm{rms}}$ reaches a steady value of $\sim 10\,\mathrm{km\,s^{-1}}$. The final value of $v_{c,\mathrm{rms}}$ depends on the evolutionary stage of the cluster as well as the total mass in the core. Note that the value of $v_{c,\mathrm{rms}}$ for runs c3f2n1 and c8f1n1 are similar, since the core masses are comparable,
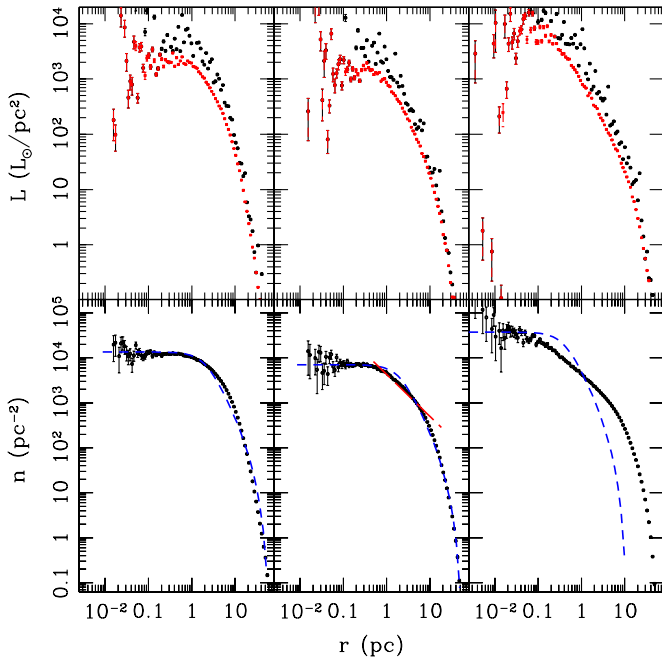
Figure 16. Radial profiles for the stellar luminosity density (top) and the stellar number density (bottom) at $t_{cl} = 12$ Gyr for models c1f3n4, c3f2n1, and at $t_{cl} = 12$ Gyr for model c8f1n1, from left to right, respectively. The error bars on each panel show the Poisson noise of the data. In the top panel, the black circles show the luminosity density for all stars taken into account. The red squares show the luminosity density taking into account only stars with stellar luminosities $L_\star < 20 \, L_\odot$. On each panel, the dashed blue line shows the best-fit King model to the data. The bottom left panel is a cluster in the slow contraction phase and is very well represented by a King density profile. The bottom middle panel is a cluster in the binary burning phase. A King profile still works for most parts, however, a hint of a power-law profile is observed (red long dash). The bottom right panel is a deep-collapse cluster showing a clear power-law profile, for which a King model is a very poor representation.

(A color version of this figure is available in the online journal.)

whereas a more massive cluster c1f3n4 shows a higher $v_{c,\mathrm{rms}}$ as expected. $v_{c,\mathrm{rms}}$ for run c8f1n1 starts to diverge from $v_{c,\mathrm{rms}}$ for run c3f2n1 only when the former reaches the deep-collapse phase.

Figure 16 shows the surface density profiles for the total luminosity and number of stars for clusters c1f3n4, c3f2n1, and c8f1n1 at the end of simulation. For each of these models, the radial positions of each star are obtained from our MC simulation. These stars are then distributed uniformly on a sphere of that corresponding radius and 2D projected distances are calculated. The whole cluster is then divided in equal logarithmic bins in the 2D projected distance and the number of stars in each bin is counted. The surface number densities are calculated by dividing the number of stars in each radial bin by the projected surface area in the bin. A similar method is adopted for calculating the 2D surface luminosity density radial profile. In each case, the error bars show the Poisson errors in each bin.

For the first two clusters, $t_{cl} = 12$ Gyr. The third suffers a deep-collapse at ~ 9 Gyr; the profile at the end of simulation is shown in that case. We find the best-fit single-mass King profile parameters minimizing the χ^2 statistic from a grid of detailed King models, solving the Poisson equation where the mass density is calculated self-consistently (Miocchi 2006, the fitting program was kindly provided by Miocchi). Since for old GGCs, and similarly for our simulated clusters, the mass range of the stars at the final stage is narrow, a single-mass King

profile is sufficiently accurate to predict the cluster parameters such as the King core radius and concentration (see Figure 16). Furthermore, we adopt a single-mass King fit since observers often follow this assumption (e.g., Dalessandro et al. 2008). The deep-collapsed cluster, c8f1n1, clearly shows a very different projected density profile compared to the other two clusters and cannot be represented with a King density profile (Figure 16). The collapsed cluster does not have a well-defined core, as seen in the steady increase in the stellar number surface density with decreasing radius. For cluster c1f3n4, which is in the slow contraction phase, a standard King density profile is an excellent representation of the simulated density profile. The density profile in the binary-burning cluster c3f2n1 is close to a King profile; however, near the central region there is a hint of a power-law density profile expected from observed core-collapsed clusters. In this region, a power law is a better representation than a King profile for this cluster indicating a self-similar collapse (Figure 16; e.g., Heggie & Hut 2003; Binney & Tremaine 2008).

We call the core radius and the concentrations calculated using the best-fit King model as $r_{c,\mathrm{obs}}$ and c_{obs}, respectively. Table 3 shows a full list of these values for all our simulated clusters. However, as shown in Figure 16, these values are not accurate for the deep-collapsed clusters. Furthermore, for the binary burning clusters a King profile may not be a good fit. Nevertheless, most of our simulated clusters are in the slow contraction phase at $t_{cl} = 12$ Gyr, where a King density profile is an excellent fit to the data. The luminosity profile is noisy due to the presence of a few high luminosity stars (Figure 16). If only stars with a stellar luminosity $L_\star < 20 \, L_\odot$ are taken into account, the profile is less noisy.

The stellar properties such as the stellar luminosity and radius for each star in the simulated cluster are calculated in tandem with the dynamical evolution of the cluster using BSE (Section 2). From the stellar luminosity and the radius the black-body effective temperature can be calculated. Figure 17 shows an example of Hertzprung–Russell diagram (HRD) obtained from the run c1f3n4 at $t_{cl} = 12$ Gyr. All binaries for this cluster are assumed to be unresolved. The effective temperature of a binary is approximated by a luminosity-weighted average. Features of a realistic HRD, including the MS, the binary sequence, giant branch, and single and binary white dwarf (WD) cooling sequences can clearly be seen. Moreover, exotic stars such as the BSSs are produced. Here, we define any MSS with a stellar mass $M_\star > 1.1 \, M_{\mathrm{TO}}$ for the cluster as a BSS and find that these stars populate the area of HRD expected from observations (Figure 18). Here M_{TO} is the MS turn-off mass for the cluster. We find that the number of BSSs in these clusters depend on the initial conditions as well as the evolutionary history. For example, clusters c1f3n4, c3f2n1, and c8f1n1 host 52, 16, and 0 BSSs, respectively, at the time when these snapshots were taken (12 Gyr for the first two and integration stopping time ≈ 9 Gyr for the third; Figure 18). A more systematic study of the correlations between the total number of BSSs and the cluster observable properties is underway.

6. SUMMARY AND CONCLUSION

We report on the recent update in the development of the Hénon based MC code CMC, developed at Northwestern. We have added the single and binary stellar evolution software of BSE (Hurley et al. 2000, 2002), in addition to the already incorporated physical processes that include two-body relaxation, strong interactions of binaries, and stellar collisions (Papers
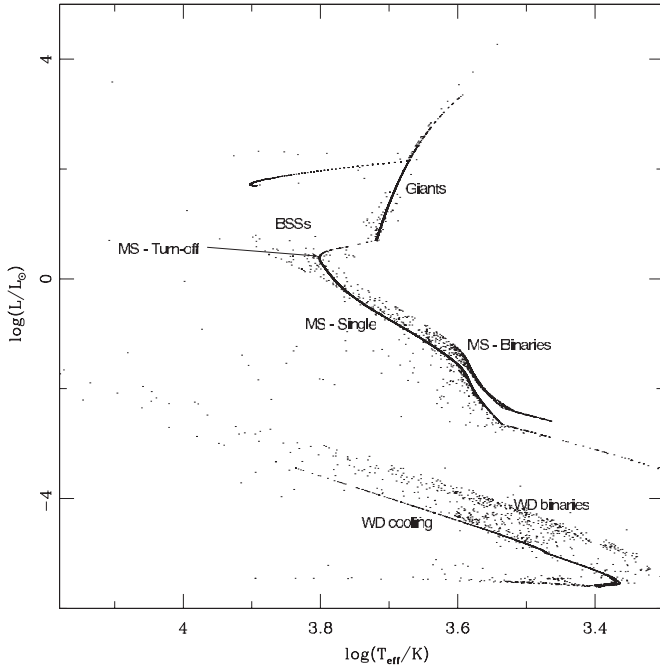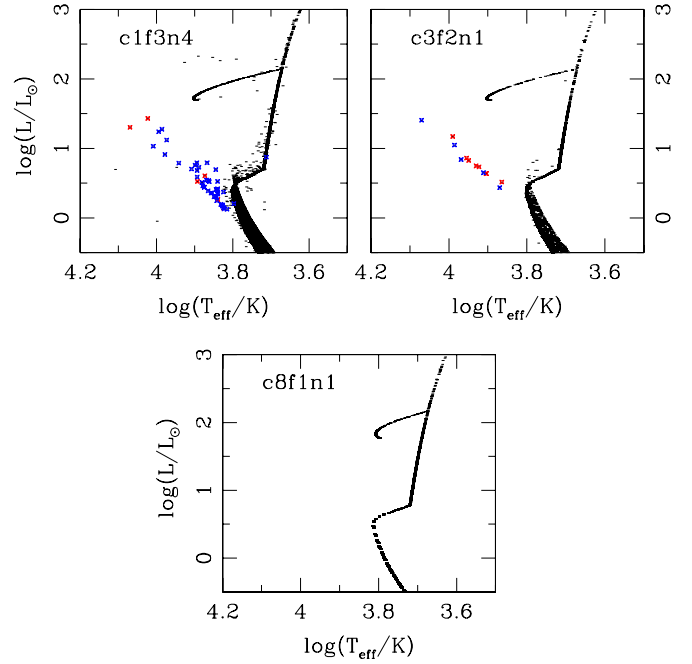
Figure 17. Example of a synthetic HRD for run `c1f3n4` at $t_{cl} = 12$ Gyr. Each dot is a bound object in the cluster (a single star or a binary). All binaries are assumed to be unresolved. The T_{eff} for a binary is the luminosity-weighted temperature. The single and binary MSs of the cluster are clearly seen. The giant branch, WD cooling sequence, and BSSs are also observed. The stars in between the single MS and the WD binary sequence are MS–WD binaries.

Figure 18. Synthetic HRD for the three sample simulated clusters `c1f3n4`, `c3f2n1`, and `c8f1n1`. For each of the HRDs, the region near the tip of the MS is shown. Each dot is one bound object (single or binary) in the cluster. The BSSs for each cluster are shown as crosses; red and blue crosses denote single and binary BSSs. Here, BSSs are defined as the MS stars with mass $m_\star > 1.1 M_{TO}$ for the cluster at its age. Cluster `c1f3n4` has a higher number of BSSs among the three example clusters (seven singles, 45 binaries) because of this cluster's higher N_i and initial f_B compared to cluster `c3f2n1` (nine singles, seven binaries). Cluster `c8f1n1` has no BSSs at this age.

(A color version of this figure is available in the online journal.)

I–IV). Thus we are now able to model realistic, dense, and massive clusters including all relevant physics with realistic stellar IMFs in our simulations. We test the code extensively and compare our results with previously published direct N-body results to validate CMC (Sections 2.3 and 3).

In spite of the differences of the basic numerical methods we find that the agreement between the CMC results and direct N-body results is excellent (see in particular Figures 1–8). The close reproduction of the evolution of the core f_b and the overall f_b warrants special mention. The evolution of f_b is related to all physical processes relevant in the cluster. Two-body relaxation drives mass segregation. Binaries, being more massive than typical single stars, mass-segregate toward the center. In the core, these binaries interact and can get destroyed via BS/BB interactions. Throughout the evolution the cluster binaries evolve and can merge or disrupt simply through binary evolution. The galactic tidal field tidally strips low mass stars from the cluster tidal boundary. Thus, obtaining the same evolution of f_b suggests that all these physical processes are implemented as correctly as in NBODY4.

There is, however, a significant advantage in using CMC to model massive clusters, in particular clusters typical for the old GGCs with significant f_b. The actual CPU time for a CMC simulation of a realistic cluster varies depending on the initial N, r_v, concentration parameter, and when the cluster reaches the binary burning phase. The dependences on N, r_v, and the concentration parameter are the usual ones—through the dependence of the relaxation time on these quantities. The dependence of the CPU time on whether the cluster is in the binary burning phase or not comes from the following. To correctly resolve the changes to the cluster properties due to the strong interactions involving binaries, we limit the number of such interactions in a single timestep of CMC. During the binary burning phase the timestep can be reduced by up to three

orders of magnitude compared to the slow contraction phase. Nevertheless, the longest run time for the simulations presented in this study is $\lesssim 7$ days on a single CPU. The quickest runs (e.g., $N \sim 4 \times 10^5$ and $f_B \sim 5\%$) take only ~ 3 days on a single CPU.

Although the core properties are accurately obtained using CMC, a larger difference is found whenever a quantity involving the total number of bound stars in the cluster is compared. For example, the agreement in the evolution of the fractional number of bound stars, although respectable (Figures 6 and 7) given the drastically different methods of simulations, can differ by up to $\approx 20\%$. These differences are dominated by the tidal mass-loss effects, which are hard to model within MC methods and can only be addressed in a criterion-based way (Section 2.3; also see, e.g., Paper IV; Giersz & Spurzem 2000). A more detailed study in characterizing the orbits in a cluster potential and tidal effects is underway, but is beyond the scope of this work.

Our results show that including stellar evolution and a realistic IMF dramatically changes the evolution of a star cluster (Section 4) and to model a realistic star cluster, inclusion of this process is vital. Early on, high stellar evolution mass-loss rates drive a cluster expansion, while later a sustained low rate of stellar evolution mass-loss significantly prolongs the slow contraction phase. Note that this dramatic difference between results obtained including stellar evolution and leaving it out is not surprising. At any given time (until the compact objects are more massive than the stars) the most massive stars in the cluster are the ones very near to the center of the cluster due to mass segregation. These most massive stars also are the ones losing mass at the highest rate. Thus at all times the mass lost due to stellar evolution is being lost from the deepest part of the cluster's potential. Depending on the initial properties

of the cluster, even without any primordial binaries the slow contraction phase may last more than a Hubble time for clusters typical for the GGCs (e.g., Figures 10 and 12). On the contrary, turning off this important effect leads to a quick contraction of the cluster due to mass segregation, even if only a moderately broad range of stellar IMF is used (Figure 10). We also show that even for simulations with a very narrow stellar mass range, for a relatively low f_b (Figure 9) the inclusion of stellar evolution can give r_c/r_h values $\approx 10\%$ larger compared to when it is left out.

One of the biggest uncertainties of studying the evolution of dense, massive star clusters is in determining the initial conditions. The detailed evolution of a cluster depends on various initial properties including the initial effective radius, mass, f_b, concentration, and the galactic tidal field. Estimating the initial conditions using the present-day observed properties of a cluster is clearly not an easy task. Moreover, starting from different initial conditions it is possible to achieve very similar present-day properties, e.g., r_c, and r_c/r_h (Figures 12 and 13). In addition, the observed present-day values can also be quite uncertain, especially the three-dimensional orbit of a cluster in the galactic potential, which is difficult to measure. Furthermore, although it may be possible to qualitatively understand individual effects of the various physical processes on the observable cluster properties, the collective effect is impossible to judge without actual detailed simulations. Thus to understand a population of dense clusters it is required to study a large parameter space and study evolution of these clusters in a realistic way including all physics in tandem.

With the recent improvement to CMC it is now possible to truly scan the full parameter space realistically without any loss of generality due to its significantly lower computational cost compared to the direct N-body codes and the accuracy and ability to treat all relevant physical processes. We have started a detailed study to create a population of realistic globular clusters, representative of the observed GGCs with a large grid of simulations with realistic initial conditions motivated by observations of young massive clusters (e.g., Scheepmaker et al. 2007, 2009). Here, we have presented some of these simulations to show that rather than creating specific clusters it is now beginning to be possible to create a whole population of GGCs using CMC with star-by-star detail. We show that using observationally motivated initial conditions, without any need for fine tuning, it is possible to create old dense clusters that are very similar to the observed GGCs (Figures 12 and 13).

Each star in CMC has realistic stellar properties such as luminosity, radius, and effective temperature in addition to the mass and the position in the cluster (which are sufficient to follow its dynamics). Hence, in addition to the global evolution of the clusters it is possible to study individual stellar populations in a cluster. For example, we show synthetic HRDs for a few simulated clusters from our grid of simulations. All features, including, e.g., the single and binary MS, WD cooling sequence, the giant branch, and BSSs, of a realistic HRD can be seen in the synthetic HRD (Figures 17 and 18). After this crucial improvement to CMC, a large array of interesting problems are now accessible. For example, a detailed study of the observed GGC BSSs, their properties, and the correlations with various cluster properties is underway.

REFERENCES

Aarseth, S. J. (ed.) 2003, Gravitational *N*-body Simulations (Cambridge: Cambridge Univ. Press)
Ashman, K. M., & Zepf, S. E. 2001, AJ, 122, 1888
Baumgardt, H., & Makino, J. 2003, MNRAS, 340, 227
Binney, J., & Tremaine, S. (ed.) 2008, Galactic Dynamics (2nd ed.; Princeton, NJ: Princeton Univ. Press)
Casertano, S., & Hut, P. 1985, ApJ, 298, 80
Chatterjee, S., Fregeau, J. M., & Rasio, F. A. 2008, in IAU Symp. 246, Dynamical Evolution of Dense Stellar System, ed. E. Vesperini, M. Giersz, & A. Sills (Cambridge: Cambridge Univ. Press), 151
Dalessandro, E., Lanzoni, B., Ferraro, F. R., Vespe, F., Bellazzini, M., & Rood, R. T. 2008, ApJ, 681, 311
Davis, D. S., Richer, H. B., Anderson, J., Brewer, J., Hurley, J., Kalirai, J. S., Rich, R. M., & Stetson, P. B. 2008, AJ, 135, 2155
Demleitner, M., Accomazzi, A., Eichhorn, G., Grant, C. S., Kurtz, M. J., & Murray, S. S. 2001, in ASP Conf. Ser. 238, Astronomical Data Analysis Software and Systems X, ed. F. R. Harnden, Jr., F. A. Primini, & H. E. Payne (San Francisco, CA: ASP), 321
Duquennoy, A., & Mayor, M. 1991, A&A, 248, 485
Fischer, D. A., & Marcy, G. W. 1992, ApJ, 396, 178
Fregeau, J. M. 2008, ApJ, 673, L25
Fregeau, J. M., Gürkan, M. A., Joshi, K. J., & Rasio, F. A. 2003, ApJ, 593, 772
Fregeau, J. M., Ivanova, N., & Rasio, F. A. 2009, ApJ, 707, 1533
Fregeau, J. M., & Rasio, F. A. 2007, ApJ, 658, 1047
Freitag, M., Gürkan, M. A., & Rasio, F. A. 2006a, MNRAS, 368, 141
Freitag, M., Rasio, F. A., & Baumgardt, H. 2006b, MNRAS, 368, 121
Giersz, M. 1998, MNRAS, 298, 1239
Giersz, M., Heggie, D. C., & Hurley, J. R. 2008, MNRAS, 388, 429
Giersz, M., & Spurzem, R. 2000, MNRAS, 317, 581
Hansen, B. M. S., & Phinney, E. S. 1997, MNRAS, 291, 569
Harris, W. E. 1996, AJ, 112, 1487
Harris, H. C., Harris, G. L. H., Hesser, J. E., & MacGillivray, H. T. 1984, ApJ, 287, 185
Heggie, D. C., & Giersz, M. 2008, MNRAS, 389, 1858
Heggie, D. C., & Giersz, M. 2009, MNRAS, 397, L46
Heggie, D. C., & Hut, P. 2003, The Gravitational Million-Body Problem: A Multidisciplinary Approach to Star Cluster Dynamics (Cambridge: Cambridge Univ. Press)
Heggie, D. C., Trenti, M., & Hut, P. 2006, MNRAS, 368, 677
Hénon, M. 1971a, Ap&SS, 13, 284
Hénon, M. H. 1971b, Ap&SS, 14, 151
Hesser, J. E., Harris, H. C., van den Bergh, S., & Harris, G. L. H. 1984, ApJ, 276, 491
Hodge, P. W. 1962, PASP, 74, 248
Hurley, J. R. 2007, MNRAS, 379, 93
Hurley, J. R., Aarseth, S. J., & Shara, M. M. 2007, ApJ, 665, 707
Hurley, J. R., Pols, O. R., & Tout, C. A. 2000, MNRAS, 315, 543
Hurley, J. R., Tout, C. A., Aarseth, S. J., & Pols, O. R. 2001, MNRAS, 323, 630
Hurley, J. R., Tout, C. A., & Pols, O. R. 2002, MNRAS, 329, 897
Hwang, N., & Lee, M. G. 2008, AJ, 135, 1567
Ivanova, N., Belczynski, K., Fregeau, J. M., & Rasio, F. A. 2005, MNRAS, 358, 572
Ivanova, N., Heinke, C. O., Rasio, F. A., Belczynski, K., & Fregeau, J. M. 2008, MNRAS, 386, 553
Ivanova, N., Heinke, C. O., Rasio, F. A., Taam, R. E., Belczynski, K., & Fregeau, J. 2006, MNRAS, 372, 1043
Joshi, K. J., Nave, C. P., & Rasio, F. A. 2001, ApJ, 550, 691
Joshi, K. J., Rasio, F. A., & Portegies Zwart, S. 2000, ApJ, 540, 969
King, I. R. 1966, AJ, 71, 64
Kroupa, P. 2001, MNRAS, 322, 231
Kroupa, P., Tout, C. A., & Gilmore, G. 1993, MNRAS, 262, 545
Lombardi, J. C., Jr., Rasio, F. A., & Shapiro, S. L. 1995, ApJ, 445, L117

Lombardi, J. C., Jr., Rasio, F. A., & Shapiro, S. L. 1996, ApJ, 468, 797
Lombardi, J. C., Jr., Warren, J. S., Rasio, F. A., Sills, A., & Warren, A. R. 2002, ApJ, 568, 939
Mackey, A. D., Wilkinson, M. I., Davies, M. B., & Gilmore, G. F. 2008, MNRAS, 386, 69
Mateo, M. 1987, ApJ, 323, L41
Merritt, D., Piatek, S., Portegies Zwart, S., & Hemsendorf, M. 2004, ApJ, 608, L25
Miller, G. E., & Scalo, J. M. 1979, ApJS, 41, 513
Miocchi, P. 2006, MNRAS, 366, 227
Noyola, E., & Gebhardt, K. 2006, AJ, 132, 447
Salpeter, E. E. 1955, ApJ, 121, 161
Scheepmaker, R. A., Gieles, M., Haas, M. R., Bastian, N., & Larsen, S. S. 2009, in The Radii of Thousands of Star Clusters in M51 with HST/ACS, ed. T. Richtler & S. Larsen (Berlin: Springer), 103

Scheepmaker, R. A., Haas, M. R., Gieles, M., Bastian, N., Larsen, S. S., & Lamers, H. J. G. L. M. 2007, A&A, 469, 925
Sills, A., Faber, J. A., Lombardi, J. C., Jr., Rasio, F. A., & Warren, A. R. 2001, ApJ, 548, 323
Sills, A., Lombardi, J. C., Jr., Bailyn, C. D., Demarque, P., Rasio, F. A., & Shapiro, S. L. 1997, ApJ, 487, 290
Spitzer, L. 1987, Dynamical Evolution of Globular Clusters (Princeton, NJ: Princeton Univ. Press)
Trenti, M. 2006, arXiv:astro-ph/0612040v1
Trenti, M., Ardi, E., Mineshige, S., & Hut, P. 2007a, MNRAS, 374, 857
Trenti, M., Heggie, D. C., & Hut, P. 2007b, MNRAS, 374, 344
Trenti, M., Vesperini, E., & Pasquato, M. 2010, ApJ, 708, 1598
van den Bergh, S., Morbey, C., & Pazder, J. 1991, ApJ, 375, 594
Vesperini, E., & Chernoff, D. F. 1994, ApJ, 431, 231